INFORMATION TO USERS

This manuscript has been reproduced from the microfilm master. UMI films the text directly from the original or copy submitted. Thus, some thesis and dissertation copies are in typewriter face, while others may be from any type of computer printer.

The quality of this reproduction is dependent upon the quality of the copy submitted. Broken or indistinct print, colored or poor quality illustrations and photographs, print bleedthrough, substandard margins, and improper alignment can adversely affect reproduction.

In the unlikely event that the author did not send UMI a complete manuscript and there are missing pages, these will be noted. Also, if unauthorized copyright material had to be removed, a note will indicate the deletion.

Oversize materials (e.g., maps, drawings, charts) are reproduced by sectioning the original, beginning at the upper left-hand corner and continuing from left to right in equal sections with small overlaps.

Photographs included in the original manuscript have been reproduced xerographically in this copy. Higher quality 6" x 9" black and white photographic prints are available for any photographs or illustrations appearing in this copy for an additional charge. Contact UMI directly to order.

ULTRASONIC CIRCUMFERENTIAL WAVES
IN EMPTY AND WATER-FILLED TUBES

Xing Li

A thesis

in

The Department

of

Physics

Presented in Partial Fulfillment of the Requirements
for the Degree of the Doctor of Philosophy at
Concordia University
Montreal, Quebec, Canada

April, 2000

0-612-54378-1

Canada

ABSTRACT

Ultrasonic Circumferential Waves in Empty and Water-Filled Tubes

Xing Li, Ph.D.
Concordia University, 2000

Ultrasonic waves propagating in the circumference of elastic isotropic cylindrical shells are theoretically and experimentally studied.

Dispersion relations of different circumferential modes, including the SH-type and Lamb-type families, are obtained by solving the wave equations numerically. Asymptotic solutions are also given for the SH-like modes.

Various technologies are applied for generating and detecting the circumferential waves. In particular, a new approach is developed for experimental determination of the dispersion of the circumferential waves in cylindrical shells. With a chirp interdigital transducer (IDT) as a broadband transmitter and receiver made on a stainless steel tube coated with piezoelectric film, both the group and phase velocities of the circumferential waves are obtained over a wide frequency range, which covers the most sensitive region of the lowest flexural mode. Other transduction approaches are also used as complementary tools in the experiments.

Experiments are carried out on both empty and fluid-loaded cylindrical shells at different frequencies. With the specially developed experimental configuration, propagation of a new flexural wave type in a water-filled tube is observed. Mode conversions are also observed between the A_0 mode in the shell and the compressional waves in the water. The results show good application potentials in liquid level sensing.

ACKNOWLEDGEMENT

Due to my limited vocabulary of phrases to express thankfulness, I just put together a list of names to whom I want to give my sincere gratitude:

Feng, my wife, without whose consistent support, encouragement and sacrifice of her time and energy, this thesis would not have been finished. **Lisa**, my first daughter, who always admires her smart father, and **Mona**, my second daughter, who has promised to write this Ph.D. thesis for her stupid dad once she is old enough for pre-school, and already offered her immediate assistance by resetting my computer just before the data were saved after hours of computation.

Prof. J.D.N. Cheeke, my supervisor who guided me throughout my M.Sc. and Ph.D. programs. Prof. Cheeke often pumps us up with his exciting new ideas, especially after an international conference. His critical comments on this thesis were extremely important.

Prof. Z. Wang, my most consulted adviser on this project, with whom I have had many valuable discussions on both the theoretical and experimental aspects. He often highlighted the significance of my findings, which sometimes might have been underestimated.

Dr. C.K. Jen, from whom I have received consistent encouragement and concrete support such as a special arrangement for me to carry out the laser ultrasound measurement in his lab.

Dr. J.-P. Monchalin, who kindly allowed me to use the optical facilities in his lab for the laser measurement. **Tony**, who provided assistance in the laser measurement and with

TABLE OF CONTENTS

LIST OF FIGURES

LIST OF TABLES

CHAPTER 1. INTRODUCTION

Recently, we have developed integrated thin walled acoustic tube wave devices which demonstrated to be an attractive mass-loading sensor candidate [1-4]. The waves can propagate either in the axial direction, or around the circumference of the tube devices, depending on the configuration of the transducers, as illustrated in Fig. 1.1. Our present interest has been focused on the circumferential waves, and in particular the lowest two Lamb-type modes (referred to as A_0 and S_0 modes, respectively), because of their special properties and potential applications in other areas. Knowledge of the characteristics of these circumferential modes is demanded for sensor device design and new application
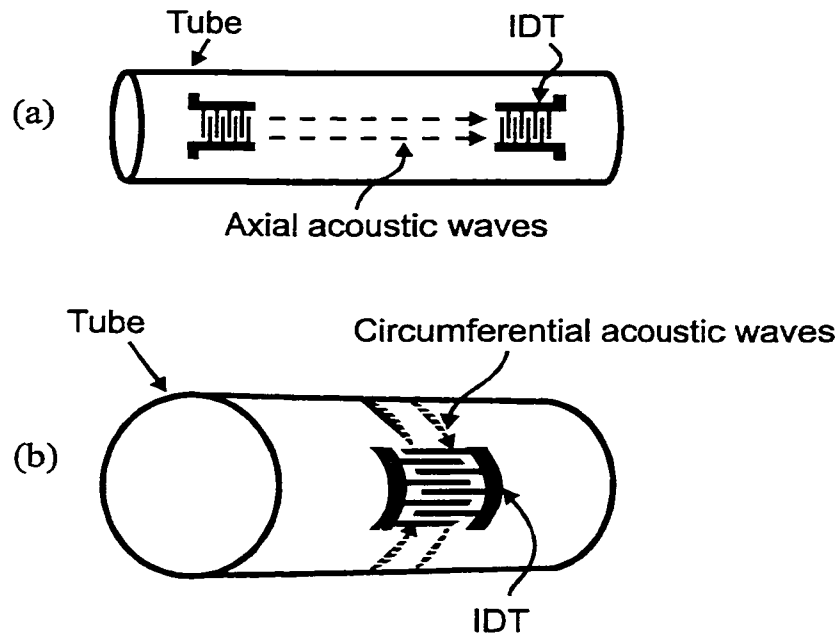
Fig. 1.1   Schematic configuration of tube wave devices

development. In our previous experiments we also observed circumferential wave phenomena which are very interesting from both the application and academic points of view. This work is in fact a continuation and extension of the previous research.

Properties of the acoustic modes in a plane plate have been extensively studied since they were first discussed by Rayleigh and Lamb a century ago [5-17]. Study of the circumferential waves in an elastic cylindrical shell, as a counterpart of the plate case, has also been carried out for decades and is still found active in recent years [18-29, 52-56].

Most of the research reported in the literature is in the context of underwater acoustics, where incident plane impinge are scattered from the cylindrical shells [20-29]. Applications are also found in non-destructive testing (NDT) such as evaluating the quality of the nuclear fuel cladding tube [36]. While extensive theoretical analysis and numerical computations based on various thin-shell models have been presented, and full dispersion curves in different cases were given, experimental dispersion curves are rarely found in the literature and usually only a few discrete points are available. Many studies have focused on problems where a cylindrical shell is immersed in a liquid (typically in water) with inside filled with air. The circumferential wave phenomenon is commonly analyzed by the resonance scattering theory (RST) [30, 31], with experimental data obtained from evaluating the measured parameters of the scattered field in the media surrounding the shell [26-29].

In liquid sensing with a tube wave device, as developed recently, the liquid is present inside the tube. There are other situations, such as a cylindrical tank containing liquid inside, where non-invasive liquid level monitoring [47] or non-destructive evaluation of the cylindrical container may be needed. However, no theoretical analysis or

2

experimental results are reported in the literature for the case where the cylindrical shell is filled with liquid inside only.

In our previous work [1], we gave a very general description of all possible modes, including the circumferential modes, in an empty cylindrical shell with finite thickness using the linear elasticity theory. We did not solve the equations. As a continuation, in this work we complete the circumferential part and solve the eigen equations for both the SH- and Lamb-type families in the circumferential modes. The lack of suitable theoretical results in the literature, based on models close to our practical cases, also motivated us to practice our own modelling, although our primary emphasis was on the experimental side. The theoretical derivations and solutions of the equations, including numeric and asymptotic results, are presented in Chapter 2.

Fig. 1.2 shows schematically the configurations of two independent families of circumferential modes. The displacement polarisation of the so called SH-type modes lies in the axial direction only, in analogy to the shear-horizontal modes in a plate. In the Lamb-type modes, the displacements are restricted within the radial-angular plane with no component in the axial direction, which correspond to the sagittal-plane in the plate case. Theoretically the SH-type modes are quite simple, but it is somewhat difficult to excite these modes in an isotropic shell. On the other hand, the Lamb-type modes can be more easily generated than the SH-type modes, at least under certain conditions, while they are much more complicated in the theoretical analysis. The same situation also pertains to their counterparts in the plate. This may also be one of the reasons that the Lamb modes in both thin cylindrical shells and plates have attracted enormous attentions

in the literature. For completeness, we give theoretical analysis on both the SH and Lamb families. Experimentally, we have focused only on the latter.

Although they have been investigated for decades, the spectrum behaviour of these circumferential modes, along with that of their plate counterparts, is not yet well
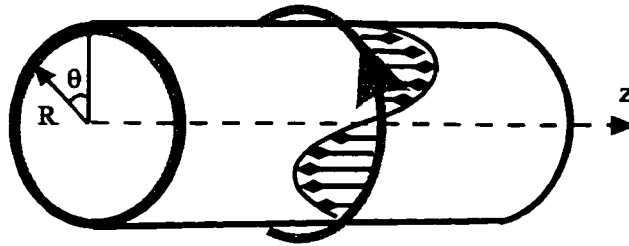
(a) SH-like circumferential wave
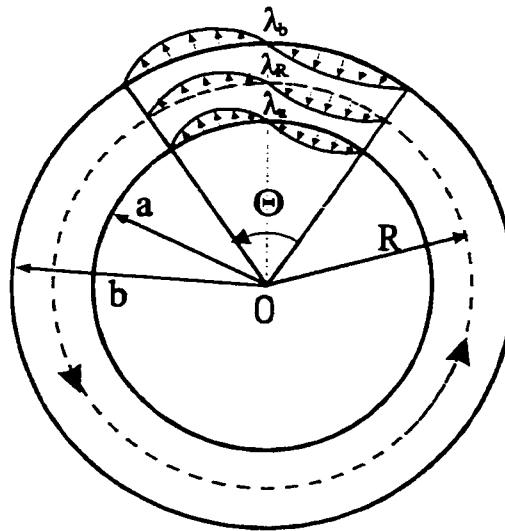
(b) Limb-like circumferential wave

Fig. 1.2 Schematic configuration of the two families of circumferential modes

4

understood. Many problems still remain unsolved and questions unanswered, especially in the fluid-loaded cases. Among the numerous theoretical dispersion curves published, whether the modes presented could actually exist in a liquid-loaded tube or not is not clear. On the other hand, a major concern, for example, has been the identification of the modes corresponding to the observed signals in particular experimental configurations.

One of our objectives in this work is to experimentally identify some of the acoustic modes which are not very clear in the literature. Technically, our effort has been made to develop a suitable approach to obtain the spectra over the most sensitive frequency range. This involves using a chirp interdigital transducer (IDT) as a broadband transmitter and receiver made on a stainless steel tube coated with piezoelectric film. The configuration is illustrated in Fig. 1.3. In Chapter 3 we give particular details on the development of this integrated wideband transducer on tubes, and how they were applied for the dispersion curve measurement. Techniques such as the pseudo-standing wave and the integration methods are also developed, in order to obtain the experimental phase velocity dispersion with this special configuration. Configurations using other types of transducers are also described, which are applied either supportively in the same cases, or independently in different cases. Chapter 3 also describes briefly the measurement arrangement and the signal processing procedures.

With the specially developed technology, dispersion curves of both the group and phase velocities were obtained over a wide frequency range. Chapter 4 presents the experimental data measured on both empty and water-loaded tubes, along with the available theoretical results for comparison and evaluation. Emphasis is given to mode identification as well as mode conversion in liquid-loaded shells, for which other

complementary experiment configurations were also used. In the discussion of the water-filled stainless steel tube, we have also included up-to-date theoretical results from the external correspondents. For the time being we will not review the theoretical background of their modelling, but compare the results with our experimental data only.
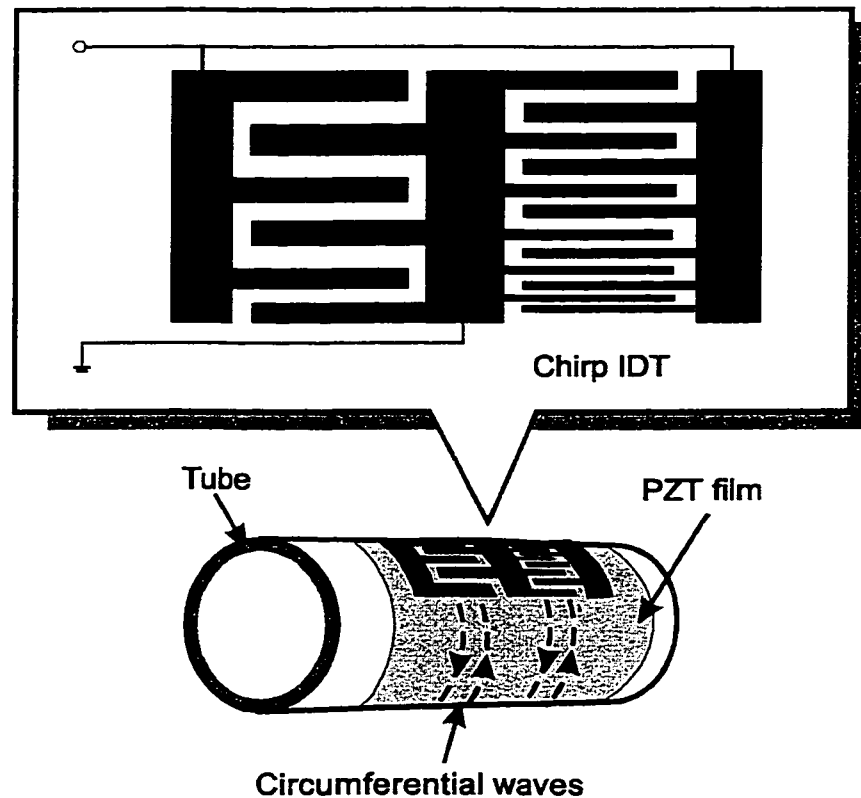
Fig. 1.3   Schematic configuration of a chirp IDT on a tube.

CHAPTER 2. THEORETICAL MODELING

2.1 GENERAL DISCRIPTION OF THE CIRCUMFEREMTIAL WAVES

Propagation of circumferential waves in a cylindrical shell is a two-dimensional problem, *i.e.* in a cylindrical coordinate system the acoustic field distributions depend only on r and θ, although the polarization can be in any direction.

In general, around the circumference either stationary or travelling waves can exist. In this work, we are interested in travelling circumferential waves in a thin-walled shell and the wavenumbers around the circumference are significantly large.

To study the net effect of a cylindrical thin shell's curvature on the travelling waves, in comparison to the case of a plate, and to avoid involving interactions between the waves themselves, it is convenient to assume that the waves travel unidirectionally around a cylindrical shell with an infinite angular interval $-\infty < \theta < +\infty$ without any overlap, in analogy to waves in an infinite plate. With this assumption, the analysis is carried out without applying the periodic boundary conditions in the θ-direction, and therefore in our solutions the wave numbers around the circumference are NOT restricted to integers or half-integers.

An alternate way to avoid the periodic boundary conditions is to assume that the waves start at $\theta = \theta_0$ and vanish at $\theta < \theta_0 + 2\pi$. Practically this can be realized, for example, by applying acoustic absorbers at a certain location to block the waves without resulting reflection. Thus the waves are unidirectional and no overlap would occur.

For a pulsed wave travelling around the circumference, the continuity condition can always be satisfied for any wave numbers without having to worry about the interference, as long as the pulse duration δt is sufficiently shorter than the period T of the wave around the circumference. This condition is easily satisfied with our experimental configuration.

In our previous work [1] we presented a very general description of all possible modes, including the axial and circumferential modes, in an empty cylindrical shell with finite thickness, using a 3-D model. It was ascertained that the circumferential waves can be de-coupled into two families of modes - the radial-angular plane modes, which correspond to the sagittal plane modes (or Lamb mode) in a plate, and the axially polarized modes, which correspond to the shear-horizontal (or SH) modes in a plate. We will refer to these two circumferential families as Lamb-type and SH-type modes, respectively. In our previous derivation, the circumferential modes were naturally separated from the 3-D problem and two independent groups of equations, one for the Lamb-type modes and one for the SH-type modes, were obtained.

In this work we solve the equations to obtain the dispersion curves and give detailed discussions for each of the families. For completeness, we first perform a brief derivation to obtain the eigen equations for the two circumferential families. Instead of using a 3-D model, we start directly with a 2-D model, without considering propagation in the axial (or z) direction.

To describe the general characteristics of the circumferential waves propagating in a cylindrical shell with a finite relative thickness, we define an **angular wave number**

$$\bar{p} = \omega / \Omega = 2\pi / (\Omega / f) = 2\pi / \Theta,$$

where Ω is the *angular phase velocity* and Θ is the *angular wavelength,* as the counterparts of the *phase velocity* and *wavelength*, respectively. Here $\bar{p}$, Ω and Θ are independent of the coordinate r. Similar to the plate waves, the wavefronts of the circumferential waves can be considered "parallel" along the angular direction at the same θ.

2.2 DECOUPLING OF THE CIRCUMFERENTIAL WAVE MODES

The equation of motion for an isotropic elastic medium, in an invariant form, is

$$\mu \nabla^2 \mathbf{u} + (\lambda + \mu)\nabla\nabla \cdot \mathbf{u} = \rho(\partial^2 \mathbf{u} / \partial t^2),$$
(2.1)

where $\mathbf{u}$ is the displacement vector, ρ is the density, λ and μ are the Lame's constants, and ∇^2 is the Laplace's operator. The displacement $\mathbf{u}$ is expressed in terms of a dilatational scalar potential φ and an equivoluminal vector potential ψ, such that

$$\mathbf{u} = \nabla\varphi + \nabla \times \psi,$$
(2.2)

where

$$\nabla \cdot \psi = 0.$$
(2.3)

The displacement equations of motion are satisfied if the potentials satisfy the wave equations

$$V_L^2 \nabla^2 \varphi = \partial^2 \varphi / \partial t^2;$$

$$V_S^2 \nabla^2 \psi = \partial^2 \psi / \partial t^2.$$
(2.4)

where V_L and V_S represent the longitudinal and shear wave velocities in this bulk material, respectively, given by

$$V_L^2 = (\lambda + 2\mu) / \rho;$$

$$V_S^2 = \mu / \rho.$$
(2.5)

In detail, the Helmholtz equations (2.4) can be expressed in cylindrical co-ordinates by

$$\left(\nabla^2 + \omega^2 / V_L^2\right)\phi = 0;$$

$$\left(\nabla^2 + \omega^2 / V_S^2\right)\psi_z = 0;$$

$$\left(\nabla^2 - 1 / r^2 + \omega^2 / V_S^2\right)\psi_r - (2 / r^2)(\partial\psi_\theta / \partial\theta) = 0;$$

$$\left(\nabla^2 - 1 / r^2 + \omega^2 / V_S^2\right)\psi_\theta + (2 / r^2)(\partial\psi_r / \partial\theta) = 0.$$
(2.6)

For acoustic waves propagating around the circumference of a concentrical hollow cylinder with finite thickness $h = b - a$, where a and b are the inner and outer radii of the cylinder, respectively, the potentials can be written in the form

$$\varphi = f(r) \cdot \cos(\bar{p}\theta + \omega t);$$
$$\psi_r = g_r(r) \cdot \sin(\bar{p}\theta + \omega t);$$
$$\psi_\theta = g_\theta(r) \cdot \cos(\bar{p}\theta + \omega t);$$
$$\psi_z = g_z(r) \cdot \sin(\bar{p}\theta + \omega t).$$

(2.7a)

or alternatively

$$\varphi = f(r) \cdot \sin(\bar{p}\theta + \omega t);$$
$$\psi_r = g_r(r) \cdot \cos(\bar{p}\theta + \omega t);$$
$$\psi_\theta = g_\theta(r) \cdot \sin(\bar{p}\theta + \omega t);$$
$$\psi_z = g_z(r) \cdot \cos(\bar{p}\theta + \omega t).$$

(2.7b)

Here, $\bar{p}$ is an arbitrary value, which corresponds to the eigenvalue $\gamma = \omega / V$ in the plate case. We will discuss their relation later. Substituting Eqs. (2.7) into (2.6), we obtain

$$\frac{\partial^2 f(r)}{\partial r^2} + \frac{1}{r} \cdot \frac{\partial f(r)}{\partial r} + \left[k_L^2 - \frac{\bar{p}^2}{r^2} \right] f(r) = 0;$$

(2.8a)

$$\frac{\partial^2 g_z(r)}{\partial r^2} + \frac{1}{r} \cdot \frac{\partial g_z(r)}{\partial r} + \left[k_S^2 - \frac{\bar{p}^2}{r^2} \right] g_z(r) = 0;$$

(2.8b)

$$\frac{\partial^2 g_r(r)}{\partial r^2} + \frac{1}{r} \cdot \frac{\partial g_r(r)}{\partial r} + \left[k_S^2 - \frac{\bar{p}^2 + 1}{r^2} \right] g_r(r) + \frac{2\bar{p}}{r^2} \cdot g_\theta(r) = 0;$$

(2.8c)

$$\frac{\partial^2 g_\theta(r)}{\partial r^2} + \frac{1}{r} \cdot \frac{\partial g_\theta(r)}{\partial r} + \left[k_S^2 - \frac{\bar{p}^2 + 1}{r^2} \right] g_\theta(r) + \frac{2\bar{p}}{r^2} \cdot g_r(r) = 0.$$

(2.8d)

where,

$$k_L^2 = \omega^2 / V_L^2;$$
$$k_S^2 = \omega^2 / V_S^2.$$

(2.9)

10

Equations (2.8a, 2.8b) are the standard Bessel equations. Their general solutions can be given by

$$f = A \cdot J_{\bar{p}}(k_L r) + B \cdot Y_{\bar{p}}(k_L r);$$

$$g_3 = g_z = C_2 \cdot J_{\bar{p}}(k_S r) + D_2 \cdot Y_{\bar{p}}(k_S r).$$

(2.10)

Where, $J_{\bar{p}}$ and $Y_{\bar{p}}$ are the first and second Bessel functions of the $\bar{p}$ th order, respectively. Subtracting (2.8b) from (2.8a) gives

$$\left[\frac{\partial^2}{\partial r^2} + \frac{1}{r} \cdot \frac{\partial}{\partial r} + k_S^2 - \frac{(\bar{p}+1)^2}{r^2} \right] \cdot \left[g_r(r) - g_\theta(r) \right] = 0;$$

(2.11),

and adding (2.8c) to (2.8d) yields

$$\left[\frac{\partial^2}{\partial r^2} + \frac{1}{r} \cdot \frac{\partial}{\partial r} + k_S^2 - \frac{(\bar{p}-1)^2}{r^2} \right] \cdot \left[g_r(r) + g_\theta(r) \right] = 0.$$

(2.12)

The solutions of (2.11) and (2.12) can be given by

$$g_1 = (1/2)(g_r - g_\theta) = C_1 \cdot J_{\bar{p}+1}(k_S r) + D_1 \cdot Y_{\bar{p}+1}(k_S r);$$

$$g_2 = (1/2)(g_r + g_\theta) = A_2 \cdot J_{\bar{p}-1}(k_S r) + B_2 \cdot Y_{\bar{p}-1}(k_S r).$$

(2.13)

The property of the **gauge invariance** can now be utilized in order to eliminate two of the integration constants in Eqs. (2.13). It may be shown that any one of the three potential components of g_i ($i = 1, 2, 3$) can be set equal to zero, without losing generality of the solution. Physically, this implies that the displacement field corresponding to equivoluminal potential g_i can also be derived by a combination of the other two equivoluminal potentials.

By setting $g_2 = 0$, one obtains

$$g_r = -g_\theta = g_1 \quad (2.14)$$

So, Eqs. (2.7) can be written in the form of

$$\varphi = f(r) \cdot \cos(\bar{p}\theta + \omega t);$$
$$\psi_r = g_1(r) \cdot \sin(\bar{p}\theta + \omega t);$$
$$\psi_\theta = -g_1(r) \cdot \cos(n\theta + \omega t);$$
$$\psi_z = g_3(r) \cdot \sin(n\theta + \omega t).$$

(2.7c)

where

$$f = A \cdot J_{\bar{p}}(k_L r) + B \cdot Y_{\bar{p}}(k_L r);$$
$$g_1 = C_1 \cdot J_{\bar{p}+1}(k_S r) + D_1 \cdot Y_{\bar{p}+1}(k_S r);$$
$$g_3 = C_2 \cdot J_{\bar{p}}(k_S r) + D_2 \cdot Y_{\bar{p}}(k_S r).$$

(2.15)

The displacement field can be obtained from Eq.(2.2), by noticing $\partial / \partial z = 0$, and given by

$$u_r = \left[f' + (\bar{p}/r)g_3 \right] \cdot \cos(\bar{p}\theta + \omega t);$$
$$u_\theta = \left[-(\bar{p}/r)f - g'_3 \right] \cdot \sin(\bar{p}\theta + \omega t);$$
$$u_z = \left[-g'_1 - (\bar{p}+1)(g_1/r) \right] \cdot \cos(\bar{p}\theta + \omega t).$$

(2.16)

It is shown in Eqs. (2.16) that the radial component u_r and the angular component u_θ are *coupled*, both involving $f(r)$ and $g_3(r)$, while the axial component u_z involves only $g_1(r)$. The physical significance is that for the free harmonic waves travelling along the circumference of a hollow circular cylinder, the solutions of the axial displacement u_z can be separated from the radial-angular plane components u_r and u_θ. Comparing to the plate case, the radial-angular plane solutions correspond to the sagittal-plane waves (or Lamb waves) and those of the axial component correspond to the shear-horizontal (SH) modes. Having shown that these two families of modes are de-coupled, next we solve them separately. We deal with the SH-type family first, which is mathematically much simpler than the Lamb-type modes.

12

2.3 EXACT AND APPROXIMATE SOLUTION OF THE SH-type MODES

By setting $f = g_3 = 0$, we have the displacement fields for the SH-type family

$$u_r = 0;$$

$$u_\theta = 0;$$

$$u_z = \left[-g'_1 - (\bar{p} + 1)(g_1 / r)\right] \cdot \cos(\bar{p}\theta + \omega t) .$$

(2.3.1)

The stress distribution is then given by

$$T_{rr} = 0;$$

$$T_{r\theta} = 0;$$

$$T_{rz} = \frac{2}{\mu}(\frac{\partial u_r}{\partial z} + \frac{\partial u_z}{\partial r}) = \sigma_{rz} \cdot \cos(\bar{p}\theta + \omega t),$$

(2.3.2)

where

$$\sigma_{rz} = \frac{\mu \cdot k_s}{2} \cdot \left\{ A \cdot \left[J_{\bar{p}-1}(k_s r) - J_{\bar{p}+1}(k_s r) \right] + B \cdot \left[Y_{\bar{p}-1}(k_s r) - Y_{\bar{p}+1}(k_s r) \right] \right\}$$

(2.3.3)

noting that $\partial u_r / \partial z = 0$.

Applying the boundary condition of free stress on the inner and outer surfaces of the shell, i.e. $T_{rz}(a) = 0$ and $T_{rz}(b) = 0$, we have the following equations:

$$\begin{bmatrix} [J_{\bar{p}-1}(x_1) - J_{\bar{p}+1}(x_1)] & [Y_{\bar{p}-1}(x_1) - Y_{\bar{p}+1}(x_1)] \\ [J_{\bar{p}-1}(x_2) - J_{\bar{p}+1}(x_2)] & [Y_{\bar{p}-1}(x_2) - Y_{\bar{p}+1}(x_2)] \end{bmatrix} \cdot \begin{bmatrix} A \\ B \end{bmatrix} = 0$$

(2.3.4)

where $x_1 = k_s a = \dfrac{\omega}{V_s} \cdot a$, $x_2 = k_s b = \dfrac{\omega}{V_s} \cdot b$ and $\bar{p} = \dfrac{\omega}{\Theta}$.

The eigenvalue $\bar{p}$ at a given frequency can be determined by solving the eigen equations

13

$$\begin{vmatrix} [J_{\bar{p}-1}(x_1) - J_{\bar{p}+1}(x_1)] & [Y_{\bar{p}-1}(x_1) - Y_{\bar{p}+1}(x_1)] \\ [J_{\bar{p}-1}(x_2) - J_{\bar{p}+1}(x_2)] & [Y_{\bar{p}-1}(x_2) - Y_{\bar{p}+1}(x_2)] \end{vmatrix} = 0 \qquad (2.3.5)$$

Dispersion relations of the phase angular velocity versus the frequency are included (2.3.5), which are not explicit. The exact solutions can be obtained only by solving (2.3.5) numerically.

In order to have an analytical understanding of the effect of the curvature on the SH-type waves, we seek asymptotic solutions for thin shells with $h / R \ll 1$.

First let us have a look at the SH modes in a plate.

For a plate with thickness h, the dispersion equation is

$$V^{(Plate)} = V_S \cdot \left[1 - \left(\frac{mV_S}{2bf} \right)^2 \right]^{-1/2}$$

$$= V_S \cdot \left[1 - \left(\frac{f_m}{f} \right)^2 \right]^{-1/2} \qquad (m=0, 1, 2, 3, ...) \qquad (2.3.6)$$

where

$$f_m = \frac{m \cdot V_S}{2b} \qquad (2.3.7)$$

is the cut-off frequency of the m-th mode, at which frequency the phase velocity becomes infinite.

For the lowest mode SH_0, the phase velocity $V_0 \equiv V_S$, and for all non-zero orders, $V_m > V_S$.

In the plate case, the transverse component (in the thickness direction) of the wave vector is $\gamma = \sqrt{k_s^2 - k^2}$. Similarly, the quantity $\beta = \sqrt{k_s^2 - \bar{p}^2 / r^2}$ in Eq (2.8b) is the radial component of the wave vector. Note here that β is r-dependent rather than a constant. For a free shell in the vacuum, β should be a real number, which requires $\bar{p} \geq k_s r$. As $h / r \to 0$, the shell becomes a plate, and the variable r can be replaced by a constant R.

Mathematically, the dispersion equation Eq. (2.3.6) for a plate is obtained from the condition

$$\gamma h = m\pi. \tag{2.3.8}$$

We can consider that the effect of the curvature of a thin shell ($h / R \ll 1$) is just a perturbation to the plate case, such that

$$\beta h = m\pi + \delta \quad (\delta \ll 1) \tag{2.3.9}$$

Our next step is to find the δ.

The minimum phase angular velocity which corresponds to the SH_0-type mode can be expressed by

$$\Theta_{min} = V_S / R, \tag{2.3.10}$$

and the corresponding angular wave number is

$$\bar{p}_{max} = k_S R = \frac{2\pi}{\lambda_S} R. \tag{2.3.11}$$

It is seen that the real eigen value should always be less than $2\pi R / \lambda_S$. It can be expected that the phase angular velocity of the lowest SH-type mode will be near the value of $\Theta \approx \Theta_{min} = V_S / R$.

15

2.3.1. Asymptotic solution

We discuss the problem starting from Eqs. (2.3.4). There are three cases, whose solutions can be obtained by different asymptotic approaches.

(i). $\bar{p} = 0$, or $\beta = k_S$. This gives pure thickness modes without any nodes along the circumference, which can be named "shear-ring" modes. We are not interested in this case.

(ii) $1 << \bar{p} < k_S r$ and $h / R << 1$

For a very thin shell ($h / R << 1$), the phase velocity can be considered to be independent of r in the shell. Thus the wavenumber β becomes approximately a constant and can be rewritten as

$$\beta^2 = k_S^2 - \bar{p}^2 / R^2 = k_S^2 - \omega^2 / V^2 \qquad (2.3.12)$$

where V is the phase velocity in the circumferential direction. The function $g_1(r)$ in Eq. (2.15) then becomes a standard zero-order Bessel equation and the solution is simply

$$g_1(r) = C \cdot J_0(\beta r) + D \cdot Y_0(\beta r) . \qquad (2.3.13)$$

The stress distribution is the same as in Eqs. (2.3.2) except that the argument is now βr instead of $k_S r$. The stress-free condition on both shell surfaces gives the homogeneous equations

$$\frac{J_1(\beta a)}{J_1(\beta b)} = \frac{Y_1(\beta a)}{Y_1(\beta b)} \qquad (2.3.14)$$

16

Note now that both variables V and ω are in the argument of the Bessel functions. The argument can be estimated by comparing with the plate case using Eq. (2.3.8)

$$\beta r \geq \gamma r = \frac{m\pi}{h}r.$$
(2.3.15)

Evidently, for any nonzero m, $\beta r >> 1$ is guaranteed as long as $r / h >> 1$. The large argument asymptotic expansions of the Bessel functions can then be applied here and, to the first order, we have

$$
\begin{aligned}
J_1(x) &\approx \left(\frac{2}{\pi x}\right)^{1/2} \cdot \left[\sin(x-\pi/4)+\frac{3}{8x}\cos(x-\pi/4)\right]; \\
Y_1(x) &\approx \left(\frac{2}{\pi x}\right)^{1/2} \cdot \left[-\cos(x-\pi/4)+\frac{3}{8x}\sin(x-\pi/4)\right].
\end{aligned}
$$
(2.3.16)

Substituting (2.3.15) into (2.3.14), we have

$$\left[1+\frac{9}{64\beta^2 ab}\right]\cdot\sin(\beta h) = \frac{3h}{8\beta ab}\cdot\cos(\beta h)).$$
(2.3.17)

Since $\beta a \approx \beta b >> 1$, (2.3.17) can be simplified to

$$\tan(\beta h) = \frac{3h}{8\beta ab} \approx \frac{3}{8}\frac{h}{\beta R^2} = \delta$$
(2.3.18)

where $R \approx a \approx b$ is the curvature radius of the thin shell.

Obviously, $\delta << 1$, so we have

$$\beta h \approx m\pi + \delta = m\pi + \frac{3}{8}\frac{h}{\beta R^2}, \quad (m = 1, 2, 3...)$$
(2.3.17)

Note that for $m = 0$, Eq. (2.3.17) gives

$$\beta R = \sqrt{3/8}$$

which does not satisfy our assumption that $\beta R \gg 1$. Than means this method is not valid for $m = 0$.

Solving (2.3.17), we have

$$\beta h \approx m\pi + \frac{3}{8m\pi} \cdot \left(\frac{h}{R}\right)^2 \qquad (m=1,2,3 \ldots) \qquad (2.3.18)$$

Comparing with the dispersion equation for the *SH* waves in a plate

$$\gamma h = m\pi,$$

the second term in the right-hand side of Eq. (2.3.18) is just the perturbation δ we assumed in Eq. (2.3.9).

It is clearly seen that the **effect of the curvature** of the shell on SH-type waves is of **second order**. As $h \mathbin{/} R \rightarrow 0$, the shell becomes a plate, and Eq.(2.3.9) reduces to Eq. (2.3.8).

Eq. (2.3.18) can be re-written as

$$\beta h \approx (1 + \delta_m)m\pi \qquad (m=1, 2, 3\ldots) \qquad (2.3.19)$$

with

$$\delta_m = \frac{3}{2} \cdot \left(\frac{h}{2m\pi R}\right)^2 \qquad (2.3.20).$$

The significance of Eq. (2.3.19) is that, by simply replacing m with $m' = m(1 + \delta_m)$ in all the dispersion relations for the SH modes in a plate, the corresponding equations for the SH-type circumferential modes in a thin shell can be readily obtained. Physically, the quantity m' represents the number of nodes in the radial (thickness) directions of the shell, which is no longer an integer as in the plate case, but increased by a small fraction

18

δ_m due to the curvature. For the m-th order mode, δ_m is approximately the square of the shell thickness over m times the shell circumference.

We can now write immediately the phase velocity of the SH-type mode for a thin shell:

$$V_m = V_S \cdot \left[1 - \left(\frac{(1+\delta_m)mV_S}{2hf} \right)^2 \right]^{-1/2}$$

$$= V_S \cdot \left[1 - \left(\frac{f_m}{f} \right)^2 \right]^{-1/2} \qquad \text{(m=1, 2, 3...)} \quad (2.3.20)$$

where

$$f_{m'} = \frac{(1+\delta_m)m \cdot V_S}{2h} = f_m(1+\delta_m) \qquad (2.3.21)$$

is the cut-off frequency, δ_m is given in Eq. (2.3.20), and $f_m^{(plate)}$ is the cut-off frequency of the m-th SH mode in a plate given in Eq. (2.3.7).

Eq. (2.3.21) shows that the cut-off frequency is increased from the plate case by a fraction of $\delta_m \sim \left(\dfrac{h}{2m\pi R} \right)^2$.

Comparing Eq. (2.3.20) with Eq. (2.3.6), we also see that the phase velocity of the SH-type modes is higher than the plate counterpart at a given frequency, noting that $f_{m'} > f_m$. In both cases, the normalized phase velocity of the m-th mode $V_m/V_S \to 1$ as $f \gg f_m$. For a given m, the difference between Eq. (2.3.20) and Eq. (2.3.6) is rapidly reduced as the frequency goes far from f_m. However, the numeric results of the exact

solution show that as f increases, the phase velocity of the SH-type modes in a shell reduces to $V_m / V_s \rightarrow 1$ much slower than that of the corresponding SH modes in a plate. The discrepancy between the asymptotic and the exact solutions is due to the fact that as $f \gg f_m$, $V \rightarrow V_s$, thus βR can no longer be a large number for any finite R, and the approximation used is not accurate. It can be expected that for the m-th mode this method is more accurate at a frequency near f_m, which is confirmed by the results of the numeric solutions.

As pointed out previously, the solution for the lowest SH-type mode corresponding to the SH$_0$ mode in a plate cannot be obtained by the method used above. The numeric solution shows that, unlike in the plate, the phase velocity of the lowest SH-type mode is not a constant, but is frequency-dependent. Only at a particular frequency f_s do we find $V_0 = V_s$. As f decreases from f_s, V_0 increases slightly from V_s. Solutions of $V_0 > V_s$ were also obtained for $f > f_s$, which shall be dropped because β must be real.

2.3.2 Numeric sulotions

The phase velocity dispersion curves of the first few SH-type tube modes obtained from the asymptotic formula Eq. (2.3.20) for a typical stainless steel tube sample are plotted in Fig. 2.1, together with the those from the numeric solutions of the exact expression Eg. (2.3.5), as well as those of the SH plate counterparts.

20
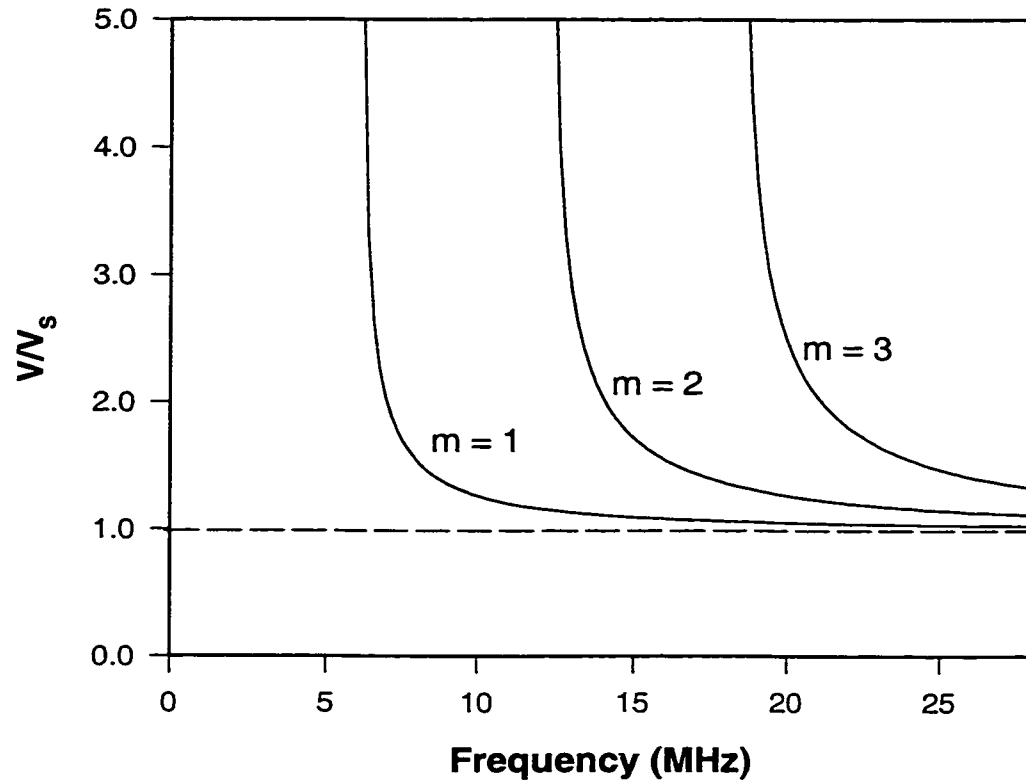
Fig. 2.1 Normalized phase velocity V/V_s of the first three non-zero order SH-type circumferential waves in a stainless steel tube with a thickness of 0.254 mm and a curvature h/R =1/20.

The difference among the three is not visible at the scale used. Fig. 2.2 shows a close-in plot for a stainless steel tube with the same wall thickness but a much larger curvature. It is seen that the second order effect of curvature is really minimal, and the asymptotic solution can give a very good accuracy, even for a tube with a curvature as large as 1/5.
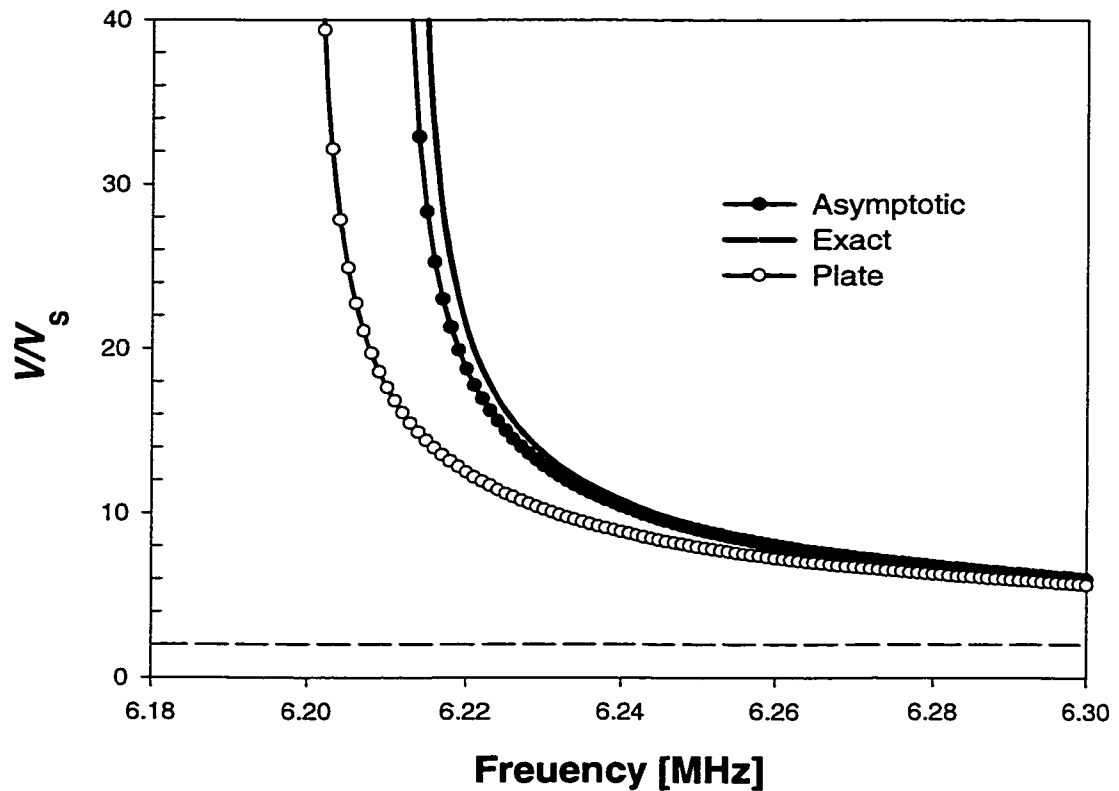
Fig. 2.2   Normalized Phase velocity of the SH_1 circumferential waves in a stainless steel tube with a thickness of 0.254 mm and a curvature h/R =1/5, compared with the corresponding SH_1 plate mode

2.4 LAMB-type MODES - EXACT SOLUTION

2.4.1 Eigen equations

For the Lamb-type family, with $g_1(r) = 0$ in Eqs. (2.1.7), we have the potentials

$$\varphi = f(r) \cdot \sin(\overline{p}\theta + \omega t);$$
$$\psi_r = g_r(r) \cdot \cos(\overline{p}\theta + \omega t);$$
$$\psi_\theta = g_\theta(r) \cdot \sin(\overline{p}\theta + \omega t);$$
$$\psi_z = g_z(r) \cdot \cos(\overline{p}\theta + \omega t).$$

(2.4.1)

and the displacements

$$u_r = \frac{\partial \varphi}{\partial r} + \frac{1}{r} \cdot \frac{\partial \psi_z}{\partial \theta} = \left[\frac{\partial f}{\partial r} + \frac{\overline{p}}{r} \cdot g_3 \right] \cdot \cos(\overline{p}\theta + \omega t);$$

$$u_\theta = \frac{1}{r} \cdot \frac{\partial \varphi}{\partial \theta} - \frac{\partial \psi_z}{\partial r} = \left[-\frac{\overline{p}}{r} \cdot f - \frac{\partial g_3}{\partial r} \right] \cdot \sin(\overline{p}\theta + \omega t);$$

(2.4.2)

$$u_z = 0.$$

The stress-strain-displacement relations are

$$\sigma_{rr} = (\lambda + 2\mu) \cdot (\partial u_r / \partial r) + \lambda \cdot \frac{1}{r} \cdot \left[\frac{\partial u_\theta}{\partial \theta} + u_r \right];$$

(2.4.3)

$$\sigma_{r\theta} = \mu \cdot \left[r \cdot \frac{\partial}{\partial r}\left(\frac{u_\theta}{r} \right) + \frac{1}{r} \cdot \frac{\partial u_r}{\partial \theta} \right].$$

Substituting (2.4.2) into (2.4.3), the stress can be given by

23

$$\sigma_{rr} = -\lambda k_L^2 \cdot f(r) + 2\mu \left[\frac{\partial^2 f(r)}{\partial r^2} + \frac{\bar{p}}{r} \cdot \frac{\partial g_3(r)}{\partial r} - \frac{\bar{p}}{r^2} g_3(r) \right]$$
$$\times \cos(\bar{p}\theta + \omega t);$$

(2.4.4)

$$\sigma_{r\theta} = -\mu \cdot \left\{ \frac{2\bar{p}}{r} \left(\frac{\partial f(r)}{\partial r} - \frac{f(r)}{r} \right) - \left(k_S^2 \cdot g_3(r) - 2 \cdot \frac{\partial^2 g_3(r)}{\partial r^2} \right) \right\}$$
$$\times \sin(\bar{p}\theta + \omega t).$$

Substituting the boundary conditions for a free shell

$$\sigma_{rr}(a) = \sigma_{rr}(b) = 0; \quad \sigma_{r\theta}(a) = \sigma_{r\theta}(b) = 0$$

(2.4.5)

into Eqs. (2.4.4), we have the eigen equation group to determine the coefficients A, B, C, and D, in the matrix form

$$\begin{bmatrix} c_{11} & c_{12} & c_{13} & c_{14} \\ c_{21} & c_{22} & c_{23} & c_{24} \\ c_{31} & c_{32} & c_{33} & c_{34} \\ c_{41} & c_{42} & c_{43} & c_{44} \end{bmatrix} \cdot \begin{bmatrix} A \\ B \\ C \\ D \end{bmatrix} = 0$$

(2.4.6)

The elements in the first two rows are:

$$c_{11} = [2\bar{p}(\bar{p} - 1) - k_S^2 a^2] J_{\bar{p}}(k_L a) + 2k_L a J_{\bar{p}+1}(k_L a)$$

$$c_{12} = -[2\bar{p}(\bar{p} - 1) J_{\bar{p}}(k_S a) + 2\bar{p} k_S a J_{\bar{p}+1}(k_S a)$$

$$c_{13} = [2\bar{p}(\bar{p} - 1) - k_S^2 a^2] Y_{\bar{p}}(k_L a) + 2k_L a Y_{\bar{p}+1}(k_L a)$$

$$c_{14} = -[2\bar{p}(\bar{p} - 1) Y_{\bar{p}}(k_S a) + 2\bar{p} k_S a Y_{\bar{p}+1}(k_S a)$$

(2.4.7)

$$c_{21} = [2\bar{p}(\bar{p} - 1) J_{\bar{p}}(k_L a) - 2\bar{p} k_L a J_{\bar{p}+1}(k_L a)$$

$$c_{22} = -[2\bar{p}(\bar{p} - 1) - k_S^2 a^2] J_{\bar{p}}(k_S a) - 2k_S a J_{\bar{p}+1}(k_S a)$$

$$c_{23} = [2\bar{p}(\bar{p} - 1) Y_{\bar{p}}(k_L a) - 2\bar{p} k_L a Y_{\bar{p}+1}(k_L a)$$

$$c_{24} = -[2\bar{p}(\bar{p} - 1) - k_S^2 a^2] Y_{\bar{p}}(k_S a) - 2k_S a Y_{\bar{p}+1}(k_S a)$$

24

where we have eliminated all the first and second order derivatives by using the recursive relations for the Bessel functions. The remaining two rows in Eqs. (2.4.6) are obtained by substitution of b for a in Eqs. (2.4.7).

For nontrivial solutions the determinant of the coefficient matrix $\{c_{ij}\}$ in Eq. (2.4.6) must be zero, from which the dispersion relations can be obtained. In the elements of (2.46), both the arguments and the order of the Bessel functions are real for the modes in an unloaded shell, if the propagation attenuation is ignored. The angular phase velocity in the order of the Bessel function, $\bar{p} = \omega / \Omega$, is the eigenvalue to be found.

Finding the asymptotic solutions for the Lamb-type modes is much more difficult and complicated than for the SH-type modes. To avoid lengthy mathematical derivations, we present only the numeric solutions.

2.4.2 Numeric solutions for an empty tube

Eqs (2.4.9) were solved numerically with a program written in Mathematica®. A typical example is given for a stainless steel tube with a wall thickness of 0.254 mm and a outer diameter of 9.8 mm. The phase velocity dispersion curves of the first few modes are shown in Fig. (2.4) by solid lines. For comparison, the dashed curves represent the dispersion curves of the phase velocities of Lamb waves propagating in a "dry" plate of the same material and thickness. It is seen that the properties of the Lamb-type circumferential waves are analogous to their plate counterparts, with only a slight difference in value due to the curvature. For simplicity we will use the same notation for

25

the circumferential waves as for the plate waves. We denote the antisymmetric modes by A_m and the symmetric modes by S_m.

Except for the A_0 mode, the phase velocity of all the symmetric and antisymmetric circumferential modes is somewhat higher than that of the corresponding plate modes at a given frequency. As for the A_0 mode, the solid line is slightly below the dashed line.

At the scale used in Fig. 2.4, such differences are not visible. More significant difference can be seen only for tubes with larger R/h values. Fig. 2.5 shows the curvature dependence of the phase velocity of the S_0 (upper plot) and A_0 (lower plot) modes at low frequencies.

In the low frequency region, there is a significant change in the dispersion curve of the S_0 circumferential mode from the plate case. While the phase velocity of the S_0 plate mode remains constant as the frequency goes to zero, that of the S_0 circumferential mode goes to infinity. In other words, the S_0 circumferential mode has a "cut-off" frequency near zero while the S_0 plate mode has none. This cut-off frequency is curvature-dependent, as easily seen in Fig. 2.5.

This result is very interesting. In Vektorov's book [11], a conclusion was given, without proof, that in an isotropic, homogeneous plate, for the symmetrical modes, when the phase velocity reaches the value of V_L, the velocity of bulk longitudinal waves, the vertical (normal to the plate surface) component of the displacement vector vanishes on the free surfaces. Pilarski et. al. [37] gave a proof of this statement, with an explicit expression for the frequency-thickness products where this vanishing occurs. In the

26
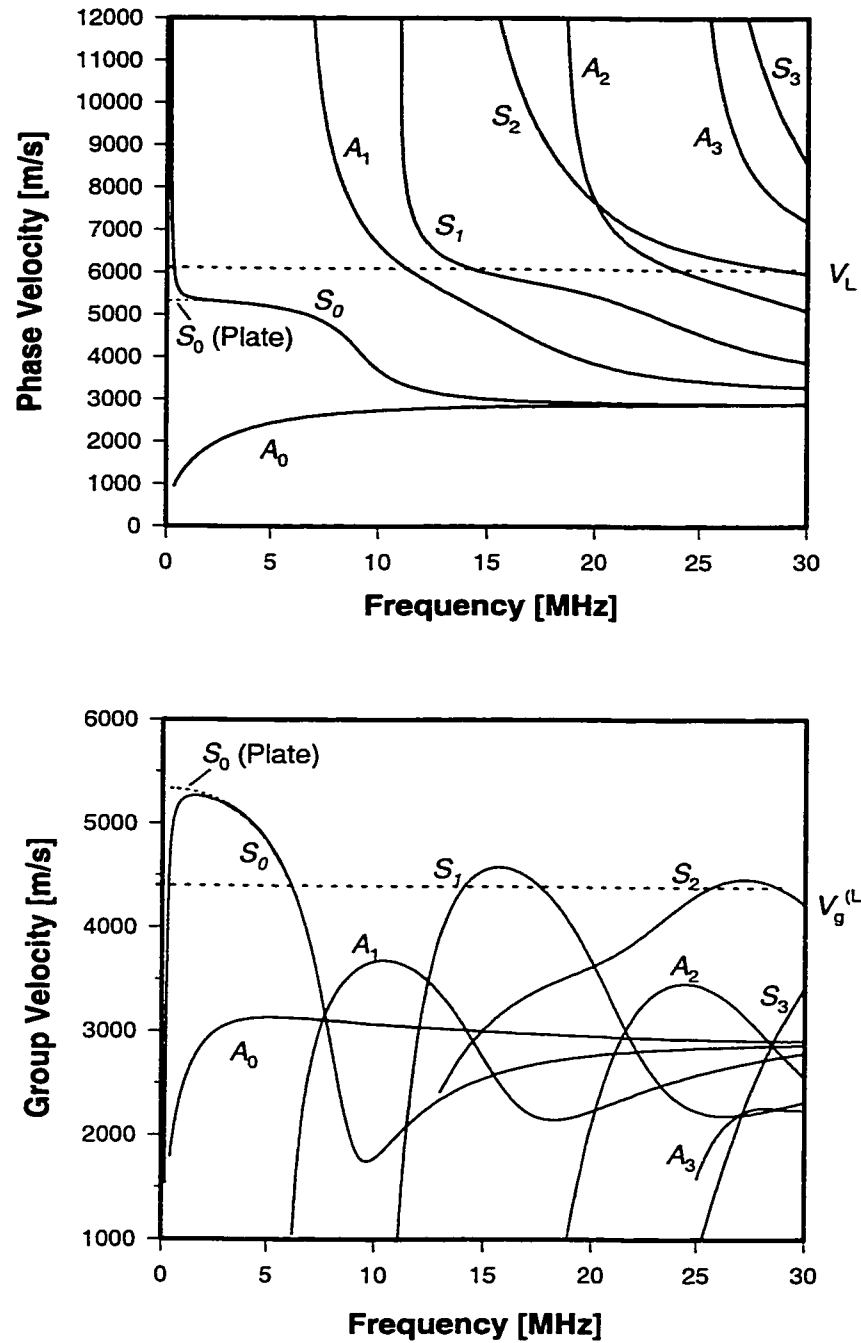
Fig. 2.3 Calculated dispersion curves of the phase velocity (upper chart) and the group velocity (lower chart) for the first few Lamb-type modes in an empty stainless steel tube, with comparison to their plate counterparts.
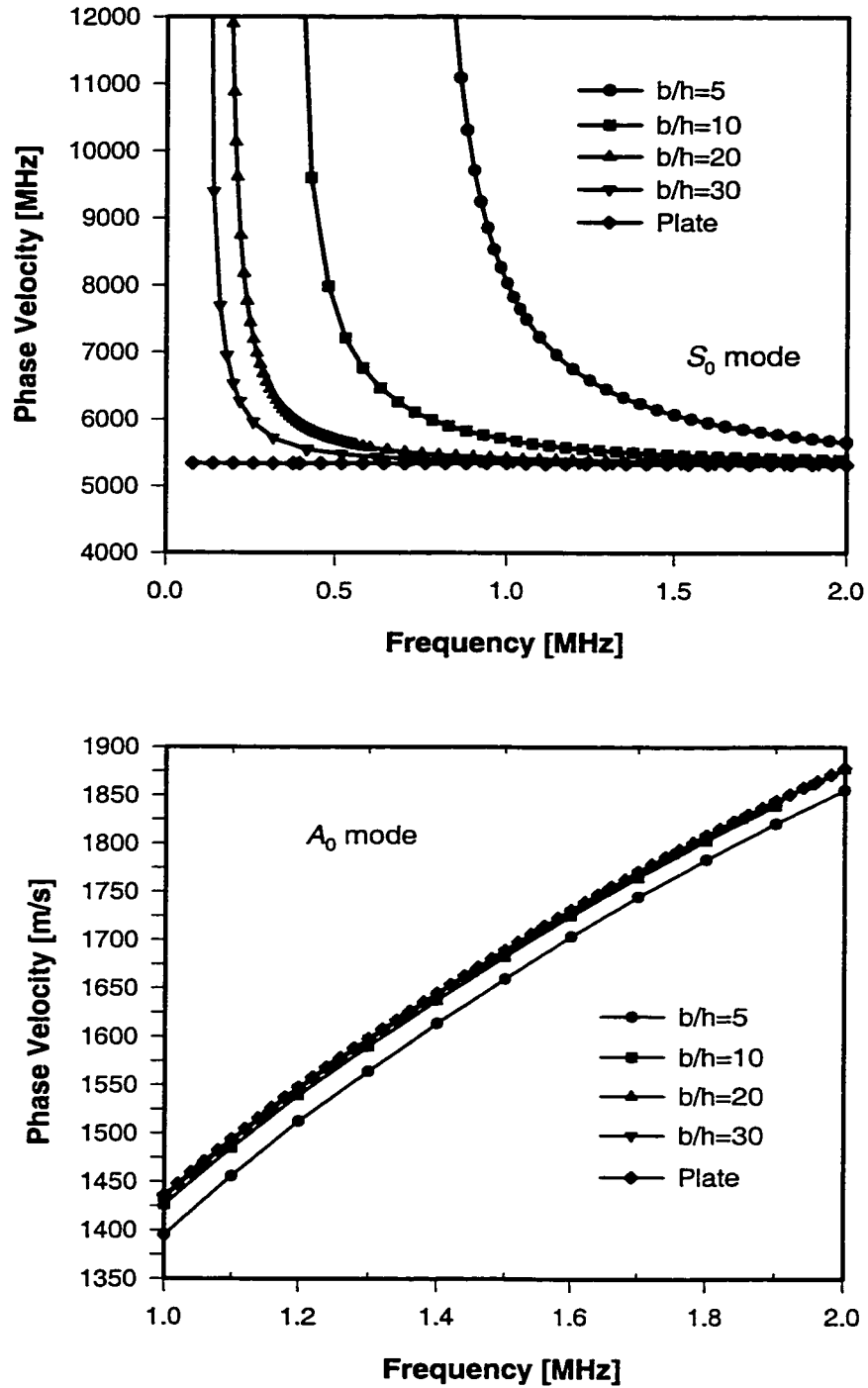
Fig . 2.4 Phase velocity of the S_0-type (upper plot) and A_0-type (lower plot) modes for empty stainless steel tubes with different curvature, where *b* is the outer radius and *h* = 0.254 mm is the wall thickness.

formula, the critical frequency-thickness product for the n-th symmetrical mode is proportional to the index n, except for $n=0$ excluded because "for zero frequency no mode with a phase velocity equal to the bulk longitudinal wave velocity exists [37]."

However, as can be seen in Fig. 2.3, in a cylindrical shell the circumferential S_0 mode does have a phase velocity equal to the bulk longitudinal wave velocity, V_L at a frequency near zero.

One can expect that for all symmetrical circumferential modes, including the S_0 mode, the radial component of the displacement vector vanishes on the free surfaces of the tube as $V \rightarrow V_L$. This prediction can be verified by substituting into Eq. (2.4.2) the $\bar{p}$ value at V_L and the corresponding frequencies in the dispersion curves. The numeric results for the first few non-zero symmetrical modes show that at the free surface $r=a, b$, the ratio $u_r / u_\theta \ll 1$ at frequencies where the phase velocity $V = V_L$.

It is demonstrated in [37] that for all non-zero order symmetrical Lamb modes in a plate, the group velocity take the same value $V_g{}^{(L)}$ at frequencies where the phase velocity $V = V_L$. In this work we have verified that this also occurs for the non-zero order symmetrical Lamb modes in a tube. However, the S_0 circumferential mode is an exception. Although in its dispersion curve there exists a point where the phase velocity $V = V_L$, at that frequency point the group velocity value obtained is somewhat different from that of the non-zero order symmetrical modes. This may be due to the inaccuracy of the numerical solution, because in this frequency range the dispersion is extremely sharp.

2.5 CIRCUMFERENTIAL MODES IN A WATER-FILLED SHELL

For a cylindrical shell filled with water, only the Lamb-type family is considered, because the water-loading has no effect on the SH-type modes. The potentials, displacements and stress in the shell take the same forms as in the empty case.

The potentials in the water are, considering only the circumferential motions,

$$
\begin{aligned}
\varphi^{(2)} &= f^{(2)}(r) \cdot \sin(\bar{p}\theta + \omega t); \\
\psi_r &= 0; \\
\psi_\theta &= 0; \\
\psi_z &= 0.
\end{aligned}
\tag{2.5.1}
$$

Substituting Eqs.(2.5.1) into the wave equation

$$
c^2 \cdot \nabla^2 \varphi^{(2)} = \partial^2 \varphi^{(2)} / \partial t^2,
\tag{2.5.2}
$$

where c is the compressional wave velocity in water, we can obtain

$$
\frac{\partial^2 f^{(2)}(r)}{\partial r^2} + \frac{1}{r} \cdot \frac{\partial f^{(2)}(r)}{\partial r} + \left[\frac{\omega^2}{c^2} - \frac{\bar{p}^2}{r^2} \right] f^{(2)}(r) = 0
\tag{2.5.3}
$$

Equation (2.5.3) is the standard Bessel functions in order $\bar{p}$ with arguments $\omega r / c = k_l r$. Its general solutions can be given by

$$
f^{(2)} = E \cdot J_{\bar{p}}(k_l r),
\tag{2.5.4}
$$

where $J_{\bar{p}}$ is the first kind of Bessel function of order $\bar{p}$. The second kind of Bessel function, $Y_{\bar{p}}$, cannot satisfy the natural boundary condition at $r = 0$, and is therefore dropped.

The displacement vector components can be obtained from the relation of

$$\mathbf{u} = \nabla\varphi + \nabla \times \boldsymbol{\psi}, \tag{2.5.5}$$

and given by

$$u_r^{(2)} = \frac{\partial\varphi}{\partial r} + \frac{1}{r}\cdot\frac{\partial\psi_z}{\partial\theta} = \frac{\partial f^{(2)}}{\partial r}\cdot\sin(\overline{p}\theta + \omega t);$$

$$u_\theta^{(2)} = \frac{1}{r}\cdot\frac{\partial\varphi}{\partial\theta} - \frac{\partial\psi_z}{\partial r} = \frac{\overline{p}}{r}\cdot f^{(2)}\cos(\overline{p}\theta + \omega t); \tag{2.5.6}$$

$$u_z^{(2)} = 0.$$

The stress-strain-displacement relations are

$$\sigma_{rr}^{(2)} = (\lambda + 2\mu)\cdot(\partial u_r / \partial r) + \lambda\cdot\frac{1}{r}\cdot\left[\frac{\partial u_\theta}{\partial\theta} + u_r\right]$$

$$= \rho_l c^2 \cdot\left[\frac{\partial^2 f^{(2)}}{\partial r^2} + \frac{1}{r}\cdot\frac{\partial f^{(2)}}{\partial r} - \frac{\overline{p}^2}{r^2}\cdot f^{(2)}\right]\cdot\sin(\overline{p}\theta + \omega t); \tag{2.5.7}$$

$$\sigma_{r\theta}^{(2)} = \mu\cdot\left[r\cdot\frac{\partial}{\partial r}\left(\frac{u_\theta}{r}\right) + \frac{1}{r}\cdot\frac{\partial u_r}{\partial\theta}\right] = 0.$$

noting that in water $\mu = 0$. Substituting (2.5.4) into (2.5.7), the stress components (omitting $\sin(\overline{p}\theta + \omega t)$) become

$$\sigma_{rr} = \rho_l\omega^2\cdot\left[J_{\overline{p}}''(k_l r) + \frac{1}{k_l\cdot r}\cdot J_{\overline{p}}'(k_l r) - \frac{\overline{p}^2}{(k_l\cdot r)^2}\cdot J_{\overline{p}}(k_l r)\right]\cdot E$$

$$= -\rho_l\omega^2\cdot J_{\overline{p}}(k_l r)\cdot E; \tag{2.5.8}$$

$$\sigma_{r\theta} = 0$$

where E is a constant to be determined. The radial distribution of the displacement components are

$$u_r = k_l\cdot J_{\overline{p}}'(k_l r)\cdot E;$$

$$u_\theta = \frac{\overline{p}}{r}J_{\overline{p}}(k_l r)\cdot E. \tag{2.5.9}$$

31

The boundary conditions are:

(1). $\sigma_{rr}^{(1)}(a) = \sigma_{rr}^{(2)}(a)$; (2). $u_r^{(1)}(a) = u_r^{(2)}(a)$; (3). $\sigma_{r\theta}^{(1)}(a) = 0$;

(4). $\sigma_{rr}^{(1)}(b) = 0$; (5). $\sigma_{r\theta}(b) = 0$ $\hspace{3cm}$ (2.5.10)

where the quantities with superscript (1) denote the stress and displacement components

in the shell, which are given by Eqs. (2.4.2) and (2.4.4).

Substituting (2.5.8) and (2.5.9) into conditions (2.5.10), we have the following equation

group to determine the coefficients, which can be written in a matrix form

$$
\begin{bmatrix}
c_{11} & c_{12} & c_{13} & c_{14} & -c_{15} \\
c_{21} & c_{22} & c_{23} & c_{24} & 0 \\
c_{31} & c_{32} & c_{33} & c_{34} & 0 \\
c_{41} & c_{42} & \cdot c_{43} & c_{44} & 0 \\
c_{51} & c_{52} & c_{53} & c_{54} & -c_{55}
\end{bmatrix}
\cdot
\begin{bmatrix}
A \\ B \\ C \\ D \\ E
\end{bmatrix}
= 0,
\hspace{2cm} (2.5.12)
$$

The nontrivial solution requires that the determinant of the matrix goes to zero, *i.e.*,

$$
\delta_w =
\begin{vmatrix}
c_{11} & c_{12} & c_{13} & c_{14} & -c_{15} \\
c_{21} & c_{22} & c_{23} & c_{24} & 0 \\
c_{31} & c_{32} & c_{33} & c_{34} & 0 \\
c_{41} & c_{42} & c_{43} & c_{44} & 0 \\
c_{51} & c_{52} & c_{53} & c_{54} & -c_{55}
\end{vmatrix}
= 0,
\hspace{2cm} (2.5.13)
$$

It is found that the elements in this matrix and those in Eq. (2.5.13) with the same indices

are identical. Here we list only the additional elements:

$$c_{15} = \frac{\rho_l \omega^2}{2\mu} \cdot J_{\bar{p}}(k_l a) = \frac{\rho_l}{2\rho} \cdot k_s^2 \cdot J_{\bar{p}}(k_l a).$$

$$c_{51} = \frac{\bar{p}}{a} \cdot J_{\bar{p}}(k_L a) - k_L \cdot J_{\bar{p}+1}(k_L a);$$

$$c_{52} = \frac{\bar{p}}{a} \cdot Y_{\bar{p}}(k_L a) - k_L \cdot Y_{\bar{p}+1}(k_L a);$$

$$c_{53} = -\frac{\bar{p}}{a} J_{\bar{p}}(k_S a);$$

$$c_{54} = -\frac{\bar{p}}{a} Y_{\bar{p}}(k_S a);$$

$$c_{55} = -\frac{\bar{p}}{a} \cdot J_{\bar{p}}(k_l a) + k_l \cdot J_{\bar{p}+1}(k_l a).$$

By setting $c_{i5} = c_{5j} = 0$ (i, j =1,2..,5), Eq. (2.5.13) reduces to Eq. (2.4.6) for the empty case.

Eqs. (2.5.13) can be solved numerically. It is worth noting that the model used describes only motions along the θ direction. The waves can be in the shell, in the water, or in both, depending on the modes and frequency range. We have ignored internal attenuation, and thus the waves propagate in either the shell or the water without consuming any energy. For the water-filled tube, no energy radiates out of the tube into the vacuum (or air), and the total energy in this closed system is conserved. So we find only real eigen values in the solution of Eqs. (2.5.13).

However, the acoustic energy can transfer between the water and the shell. Radiation from one subsystem to the other and conversion from one mode to another can occur. In this case, the waves are "leaky" if we consider the subsystems separately, and the propagation of the waves may not be purely circumferential. For simplicity we will use the quasi-plane wave approximation and the acoustical ray method in our analysis of

the radiation and the associated mode conversion, which will be discussed in Chap. 4.2. with our experimental observations.

2.5.2 Numerical results for a water-filled tube.

Solving numerically Eqs. (2.5.13) for a water-filled tube, we obtained two sets of dispersion curves. While solutions corresponding to the Lamb-type modes are still found, and remain nearly unchanged from the empty case for a thin shell, an additional series of modes are also obtained. Fig. 2.5-(a) shows the dispersion curves for a water-filled stainless steel tube of the same size as that presented in Section 2.4.2.

For the frequency range given, we see that in addition to the A_0 and S_0 modes, there are many new modes not found in the empty tube. The dispersion of these additional modes coincide with that of the so called "Whispering Gallery" modes confined in the cylindrical water column by the tube wall, obtained with the resonant scattering theory [55, 56]. There are two types of Whispering Gallery modes in a liquid filler; one is with a rigid boundary and another with a "soft" boundary. Our results corresponded to the second Whispering Gallery type. In our case the water column is within a tube wall that has finite density, and is "free" to vibrate. We label these modes with W_m (m=1,2,3 ....). Both the rigid type and soft type Whispering Gallery modes in a layer of a liquid filler propagate at the cylindrical liquid-solid boundary without attenuation. In other words, the roots of the eigen functions are all real, which is the same as in our case.

Fig. 2.5-(b) shows the group velocity dispersion curves of the water-filled tube modes. Comparing Fig. 2.5 -(a) and -(b), we see that for each W_m mode, except for $m=1$,

34

the group velocity reaches its maximum value V_g^{max} at the cut-off frequency, where the phase velocity goes to infinity. This maximum value is a constant for all W_m modes with m>1. For the typical stainless steel tube sample, $V_g^{max} \approx 2420$ m/s.

Very recently, Veksler *et al.* [55] and Maze [56] observed in their theoretical modelling by the resonant scattering theory, a third mode family in a liquid filled tube, in addition to the Lamb-type and the Whispering Gallery type modes. With our modelling based on the classical linear elasticity theory, we have by far not found any roots for these new modes from the eigen equations. In Chap. 4.1 we also compare our experimental results with the theoretical ones in [55, 56].
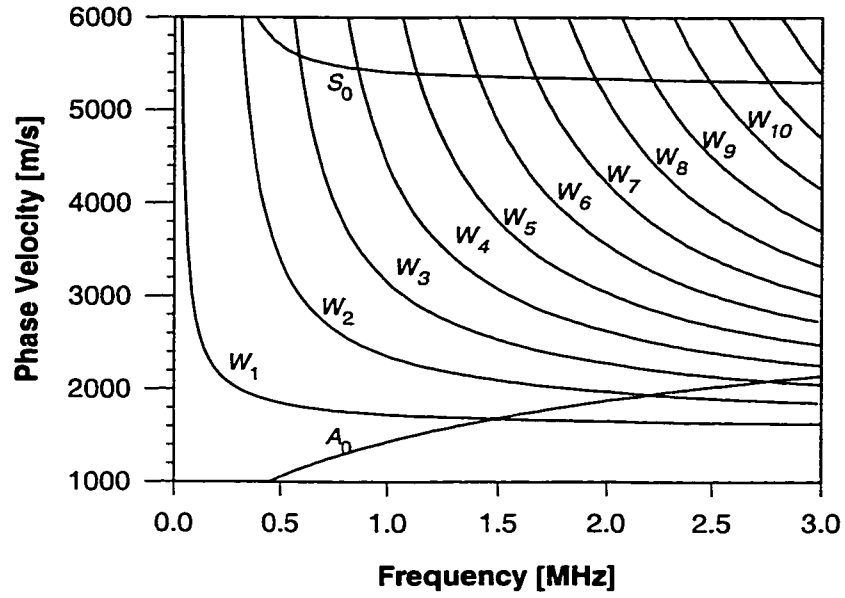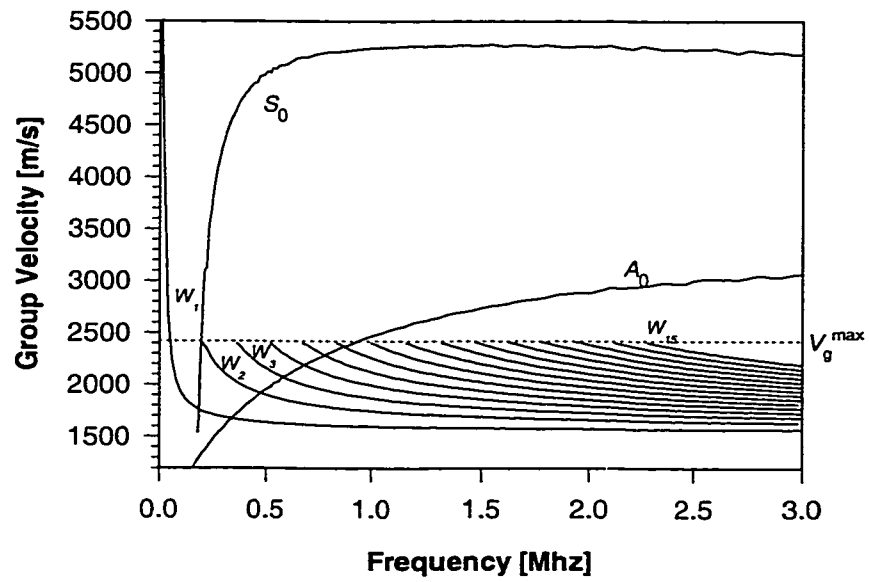
Fig. 2.6 Calculated dispersion curves of (a) the phase velocity and (b) the group velocity of the circumferential modes in a water- filled stainless steel tube.

36

CHAPTER 3. EXPERIMENTAL METHODS AND PROCEDURES

3.1 TRANSDUCTION TECHNOLOGIES

Proper transduction configurations are crucial in order to effectively generate and detect the circumferential waves. While our emphasis is given to the integrated configuration, two other approaches are used in this work. The three different approaches are applied either independently in different cases, or supportively in the same cases as complementary tools.

3.1.1 Integrated method– Interdigital Transducer (IDT)

In our R & D of thin-walled tube sensor devices, we developed a special technology of making transducers directly on the tube surface. Piezoelectric PZT films were coated on the outer surface of the tubes, and interdigital transducers (IDT) were then fabricated on top of the piezoelectric film. This technology not only made the novel thin-walled tube wave devices a promising sensor candidate, but also provided a very useful tool in investigating circumferential waves.

With this configuration, circumferential waves can be effectively excited and very well guided around the circumference, as illustrated in Fig. 1.1, which gives excellent signal-to-noise ratio in the received signals. Because the IDT electrodes were very thin compared to the tube wall (typically 1:1000), perturbation introduced by the transducer is minimal. Since the transducer is integrated on the tube surface, it has no alignment problem, and thus provides more consistent results for measurements under different conditions. The most significant feature is that, when IDTs with varied spacings (so

called "chirp" IDTs) are used, as will be described later, circumferential waves over a wide frequency range can be generated and detected continuously, which is particularly desirable for dispersion curve measurement. This is the superior advantage of this technology over the others.

This method also has its own limitations. Only selected materials are suitable for PZT coating, and the tube size is limited. In addition, highly specialized skills are required for the device fabrication, and good devices are not easy to obtain.

A. Fabrication process

The key technology in this approach is coating piezoelectric films onto the tube surface, which convert electrical energy into mechanical energy and the reverse. A specially designed recipe of the stock solution [1] was used for dip-coating PZT films on metallic tubes. A typical tube substrate was a stainless steel tube with a diameter of 9.8 mm and a wall thickness of 0.25 mm. Aluminium tube samples were also made. Before coating, the tube substrate was cleaned, and then pre-heated to a temperature of about 500 °C to further remove possible remaining organic substance. The pre-heating could also form a thin oxidation layer on the stainless steel tube surface, which could enhance the adhesion between the substrate and the ceramic PZT film.

A step motor-controlled system was used for the dip-coating. The tube substrate was kept vertical by the sample holder, and immersed in the chemical solution by a depth of the desired coating length. It was then lifted slowly and smoothly at a speed of about 1.5 cm/min, as programmed, until the whole tube was out of the solution. A thin gel layer was formed on the outer surface of the tube. After drying in the air for about 10 minutes,

the tube sample was placed in a vertically mounted tube furnace. The firing of the film was carried out at a temperature of 480 °C for 12 minutes. The sample was then taken out, staying in the air until it cooled down to the room temperature. By repeating the above procedure, multiple layer coating was performed and films of up to 20 layers were obtained. The as-fired films coated on the tube were annealed at 620 °C for 2 hours for the crystallization.

The as-annealed film is not piezoelectric and poling of the film is required. The PZT films coated on the tubes were poled in a conventional way by applying a DC voltage across the film thickness, using the conductive tube itself as one electrode and an aluminium layer on top of the PZT film surface as the other (Fig. 3.1 (a)). The aluminium layer was also used later for IDT fabrication. The sample was kept at 185 °C for 2 hours with an applied DC voltage of about 3 V per 1 mm of PZT film thickness, and then slowly cooled down to room temperature. The DC voltage was withdrawn as the temperature dropped below 60 °C.

An alternate poling configuration was also used which was carried out after the IDT electrodes had been fabricated on the PZT film. In this case the DC voltage was directly applied across the IDT fingers, as illustrated in Fig. 3.1 (b). In this case, higher DC voltage was applied. This method was found particularly useful for reducing the short-circuit risk during the poling due to micro-defects in the PZT films. Films free of micro-defects were very difficult to obtain, especially for large area coating. Aluminium deposited on the PZT film surface could penetrate through the micro tunnels and resulted in a short-circuit between the top and bottom electrodes. At the points which were not short-circuited, but weakened by the micro-defects, electrical breakdown could happen

39

when a high DC voltage was applied. Breakdown could also happen if the film thickness

was not uniform over a large area. With the conventional poling configuration shown in

Fig. 3.1-a, only one defect spot could kill.

It is noticed that most of the top aluminium layer will be etched out including the

unused area and the IDT finger intervals. So limited micro-defects in the whole film area
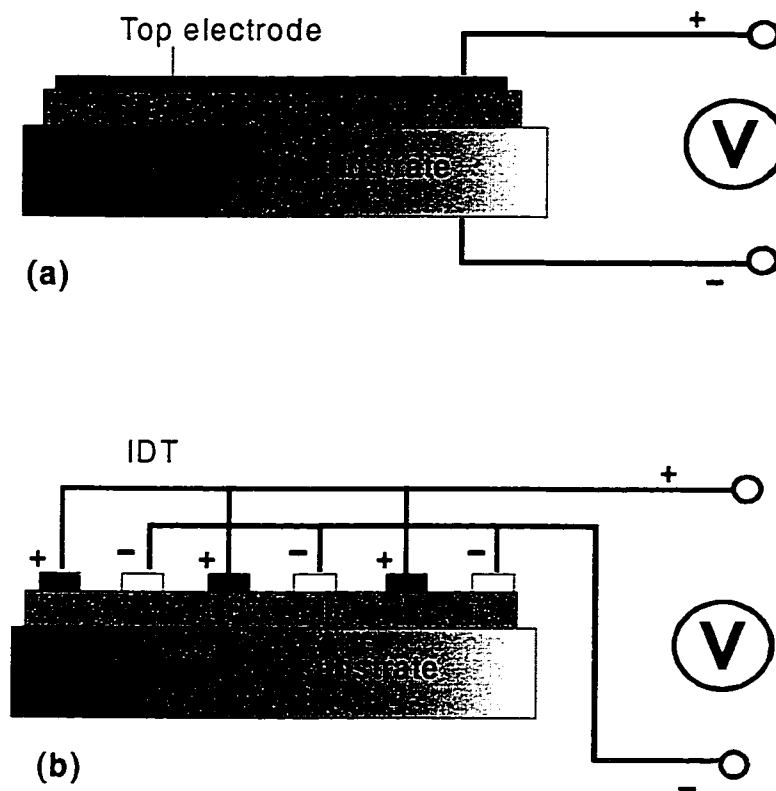
Fig. 3.1   Two configurations for PZT film poling

they have a good probability to distribute out of the usable area or just reside in the spacines between the IDT fingers, rather than exactly under the IDT fingers. So the risk of short-circuit could be much reduced. Even if there happen to be some micro-defects exactly under a few IDT fingers which would cause a short-circuit between those particular IDT fingers and the tube, a short-circuit may not have to just happen between the IDT electrodes themselves. Since in our case the finger spacing was much larger than the PZT film thickness (~200:1), the electric fields generated from the poling voltage applied across the IDT fingers were still mainly in the "vertical" or the film thickness direction rather than in the "horizontal" or the surface direction. Therefore, a breakdown between a positive-negative finger pair is also unlikely for films without a uniform thickness. In the event that a breakdown happens between the tube and a few IDT finger, the majority of the IDT could still survive and function well as long as such breakdown does not happen for both a positive and a negative electrode at the same time.

In order to fabricate the IDT patterns on the curved surface of a tube, flexible masks made of transparent films were used. After a thin aluminium layer (typically 2000 Å) was deposited on the PZT-coated tube surface by means of vacuum evaporation, a photoresist layer was then applied on the tube using the same dipping technique as for the PZT film coating. Following this was a standard wet-etching procedure commonly used in the photolithography process for planar structures.

B. Chirp IDT

For an IDT with uniform finger spacing, the center frequency is determined by the finger period P which is approximately the wavelength, and the bandwidth depends on the

number of electrodes N. For a chirp IDT with varied finger spacing, the bandwidth mainly depends on the variation of the local period P_n of the electrodes. Fig. 3.2. shows schematically the geometry and impulse response of a chirp IDT.

Consider the chirp IDT as a receiver. In coming acoustic waves will have maximum efficiency in generating an IDT voltage in the region where the finger period is also that of the incoming wave. The same situation also holds when the IDT acts as a transmitter. Acoustical waves will be principally excited by regions of the IDT whose
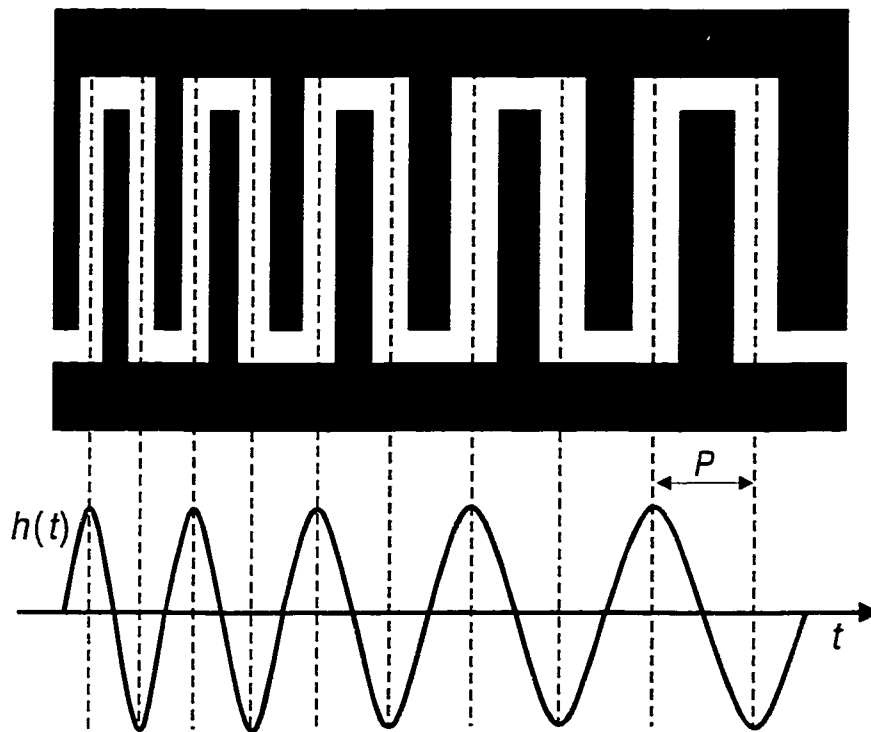
Fig. 3.2   Schematic geometry and impulse response of a chirp IDT

42

finger periods are in synchronism with the excitation frequency. For a chirp device with center frequency f_0 and bandwidth B, the excitation frequency at the "low end" and of the IDT, *i.e.* maximum finger spacing, will be $(f_0 - B/2)$, while that at the "high end", i.e. minimum finger spacing, will be $(f_0 + B/2)$.

It is noticed that in a two-port configuration, either up-chirp or down-chirp, the distance from the IDT finger pairs in the transmitter to their counterparts in the receiver varies with different finger spacings, as shown in Fig. 3.3 (a). Therefore the time delay between the two ports is frequency-dependent.

One would immediately question how this configuration can be used for dispersion measurement, if it itself is already dispersive. This is true if a two-port structure is used, as shown in Fig. 3.3 (a). However, for a single chirp IDT as a transmitter and receiver along the circumferential direction of a cylinder, this inherent dispersion *does not* exist for constant wave velocity. At first glance one would think that the one-port chirp IDT should be up-chirp dispersive in one direction, and down-chirp dispersive in the other direction, similar to the two-port cases in Fig. 3.3 (a). A careful examination shows that this is not the case. As shown in Fig. 3.3 (b), the distance an acoustic signal travels in either direction from the transmitter back to itself as the receiver is a constant for any finger pairs of any spacing, which is nothing but the circumference of the shell. Thus there should be no dispersion in the time delay, unless the velocity of the acoustical circumferential waves is dispersive. This justification was experimentally verified by comparing the measured time delay at several frequency points with those obtained with other methods.

43

Doubly-dispersive up-chirp

Doubly-dispersive down-chirp

(a)
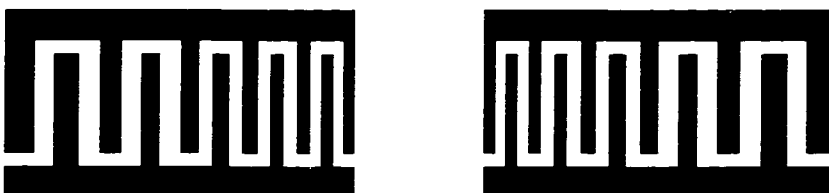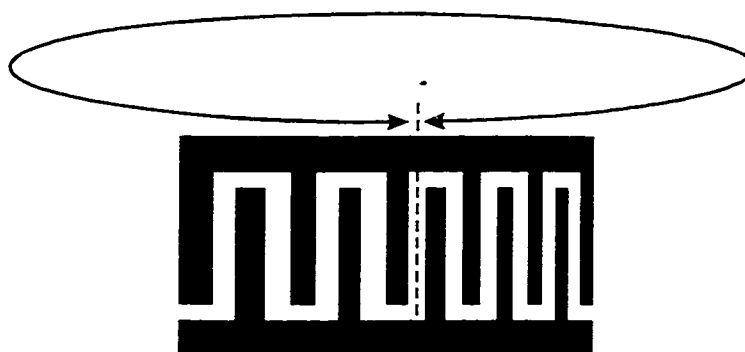
Single chirp IDT along tube circumference

(b)

Fig. 3.3   Comparison of a one-port chirp IDT on a tube surface and two-port chirp IDTs on a planar surface.

For best results in both the electrode layer deposition and the photolithography procedure, the total IDT length should not exceed 1/3 of the tube circumference, *i.e.* $N \cdot P \leq \frac{2\pi R}{3}$. This condition limits the total number of the electrodes N for given finger spacings. While for a uniform IDT the maximum N limits the minimum attainable bandwidth, for a chirp IDT it limits the maximum attainable bandwidth for a given increment in the finger spacing P, or the minimum increment in P for given bandwidth. There was then a trade-off between the bandwidth and the increment ΔP. Since our objective was to obtain detectable signals, the actual shape of the frequency response is not very important, as long as the signal is at an acceptable level over the desired frequency range. So we sacrifice ΔP to maximize the bandwidth B.

For a typical stainless steel tube sample with a wall thickness of 0.25 mm and diameter of 10 mm, the finger spacing variation is estimated to be approximately from 0.4 mm to 1.6 mm, in order to cover the desired frequency range, based on the theoretical dispersion curve (see Fig. 4.2).

In order to meet all the requirements and keep a minimum required N, we split the IDT into parallel IDTs, as illustrated in Fig. 1.3.

3.1.2. Contact method - piezoelectric thin disk transducer

This method is simple, straightforward, economic and quite effective. It can be applied to shells made of any materials which support acoustic waves, and there is no upper limit on the shell size. Commercially available thin-disk piezoelectric transducers were used. This type of transducer is commonly used for generating bulk waves, so it is also often called

bulk wave transducer. The transducer was aligned tangentially with the tube, with a thin layer of acoustic couplant applied between the transducer and the tube. Ideally, the acoustic couplant applied should be a very narrow and straight line parallel to the tube axial direction, so that the transducer can be considered as a "line source". The narrowness, straightness and parallelness (to the axial direction of the tube) of this line coupling layer is very important to get sharp "echoes", in order to effectively excite the circumferential waves and to minimize the error of the time delay measurement.

There are a number of disadvantages of this method:

A number of transducers of different nominal frequencies are needed to get the spectrum. Only limited discrete frequency points can be obtained. Careful alignment (re-alignment) is required in each experiment. There is larger perturbation on the experiment sample. It is not suitable for shells of small diameters, especially at low frequencies.

3.1.3 Non-contact method - laser probe

This technology can be used for very wide frequency range, and can provide continuous spectra if used to generate the waves. However, as a generator a very high power laser source is required, which was costly and not available in our case. We used a low power laser source for detecting only. Since this method is non-contact, and passive when used for receiving only, no modification is made on the experiment sample. The disadvantage is that the signal-to-noise ratio is usually poor. Other concerns are the elegant optical alignment required and the demanded reflective material surface of the sample.

46

Most interferometric systems described in the literature for laser ultrasound applications detect the ultrasonic motion perpendicular to the surface of the specimen when the beam is sent normal to it. As described by Monchalin [39], these systems are based on either optical heterodyning, which is the case of most of theirs and of ours as well, or velocity interferometry. In the optical heterodyning technique, the light scattered by the surface of the specimen is made to interfere with a reference wave derived directly from the laser. The interferometric arrangement used in this case is called homodyne if the reference wave and the wave sent onto the specimen are at the same optical frequency, or heterodyne if one of the waves is frequency offset with respect to the other. In the velocity interferometry technique, an interferometer giving time delay between the interfering waves demodulates the frequency shift of the scattered light produced by the surface motion. Such techniques permit determination of only one component of the ultrasonic surface motion. This is sufficient for many applications, in which the detection of the arrival of the ultrasonic wave is the only requirement, as for our case.

In our experiment an OP-35-O optical probe system was used. Its frequency response bandwidth extends from 1 KHz to 35 MHz. This instrument is based on optical heterodyning, which consists in beating (or making to interfere) the beam scattered or reflected by the surface with a reference beam, both being derived from the same laser. In order to ease calibration and establish immunity to ambient vibrations, which generally produce displacements exceeding the small ultrasonic displacements to be detected, the reference beam is frequency shifted with a Bragg or acoustic-optic cell (by 40 MHz in our case). The electronic demodulation circuitry produces a voltage signal output proportional to the surface displacement, unaffected by the environmental vibrations. The instrument

47

uses a small 5mW He-Ne laser as the laser source. This laser produces several

longitudinal modes separated in frequency by c/2L, where c is the speed of light and L is

the laser cavity length.

Fig. 3.4 illustrates the configuration of the contact method combined with the non-

contact laser probing method.
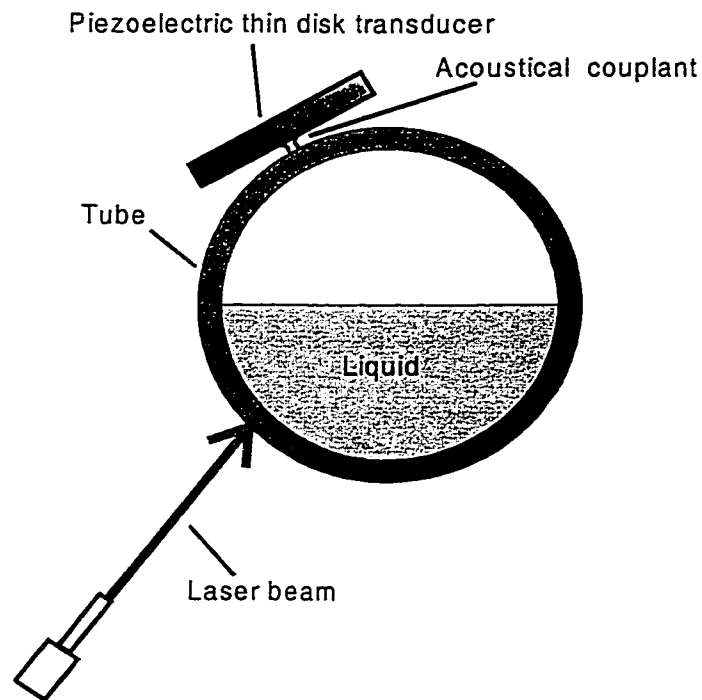
Fig. 3.4 Schematic configuration of the contact method using a piezoelectric thin disk transducer and the none-contact method using a laser beam.

Note that the laser probing position is such that the distance from the contact point of the thin-disk transducer in one direction is about half that in the other direction. This is to well separate the two echoes from the two directions. In this configuration the echo trains received by the laser probing contains two echo series, with equal time interval but different delay time and probably different amplitude.

3.2 METHODS FOR VELOCITY MEASUREMENT

3.2.1 Group velocity - time delay measurement

a) One-port or two-port

Experimentally, the group velocity can be determined by measuring the time delay of the acoustical signals travelling around the circumference. In our theoretical modelling in Chapter 2, we assumed that the waves could propagate around the circumference without any overlap and no interference would be involved. In reality, one must face the overlapping problems. One simple solution is to use pulsed waves instead of continuos waves (CW). Standing waves would not be formed as long as the duration of the pulse is sufficiently short compared to the period for the waves to propagate around a complete circumferential cycle, even if the waves are allowed to propagate in both directions around the circumference. Although the two branches of waves in opposite directions will meet after travelling one or more complete circumference(s), a short-period overlapping would not support a formation of standing waves. For short duration pulses, the two branches of the waves in the opposite directions can meet at only two positions: the initial point where the transducer is located, and the point which is exactly half way around the

49

circumference. At either of these two positions the superposition is always constructive, which can only enhance the received signals, since any two branches of waves of the same mode are always in phase when they meet after travelling exactly the same path length (n or n+1/2 times a complete circumference).

In a two-port (transmission) configuration, the time interval is determined by two transducers separated by a distance in the path, one as the transmitter and another as the receiver. In a one-port (reflection) configuration, a transducer generates the signals and receives the echoes, *i.e.* the acoustical signals reflected from a boundary in the path.

One advantage of the reflection configuration is that the length of the acoustical wave path can be extended by many folds, so that accuracy of the time delay measurement can be significantly increased. This is especially useful in the cases where the acoustical path is extremely short, such as crossing the thickness of a thin film. Another advantage of this configuration is that the electromagnetic (EM) feedthrough can be completely eliminated. Since electromagnetic waves travel at the speed of light which is greatly much faster than the acoustical waves, and they attenuate much more rapidly than the latter in most media, the EM feedthrough signals no longer appear after the first received acoustical echo. The time interval between the subsequent echoes is used, which provides better accuracy than using that between the initial signal and the first echo. Usually in a two-port structure only the latter is available. Given the fact that the circumferential waves can naturally come back to the transducer, for either a one-port or a two-port configuration, multiple echoes are available. However, unless the two transducers are perfectly symmetrical, *i.e.* they are equally spaced in both directions around the circumference, each received echo will split into two because of the different

delays from the two opposite directions. This would reduce the resolution in the time interval measurement, unless the signals of the two branches are either well separated or totally coincide at the receiver.

When we used the laser probe as a passive detector, the probing point was chosen at about 1/3 of the tube circumference from the generating point, as illustrated in Fig. 3.4, so that the time interval of the two wave branches were very well separated.

As discussed later in 3.1.1 B, for the broadband measurement using a chirp IDT as the transducer, only one-port configuration is suitable.

b) Cross-correlation

The precise determination of the time delay is based on the cross-correlation of consecutive echoes. Cross-correlation time delay measurement has been used successfully with conventional ultrasonic techniques [CR1], giving the most reliable and reproducible results even in difficult cases where the echoes could be very noisy and distorted. The cross-correlation of two time domain signals $u(t)$ and $v(t)$ is defined by

$$C_{uv} = \lim_{T \to \infty} \frac{1}{T} \int_0^T u(t)v(t + \tau)d\tau \qquad (3.2.1)$$

The time delay measurement by cross-correlation is based on the property that the auto-correlation $C_{uu}(\tau)$ of a signal $u(t)$ is an even function of τ, which is maximal at $\tau = 0$. If $v(t)$ is the signal $u(t)$ delayed by T, i.e.

$$v(t) = u(t-T), \qquad (2)$$

the cross-correlation function $C_{uv}(\tau)$ will be the auto-correlation function $C_{uu}(\tau)$ shifted by T, *i.e.*

$$C_{uv}(\tau) = C_{uu}(\tau\text{-}T)$$

and will therefore have its maximum at $\tau = T$.

Two portions in the received echo train, each including one of these arrivals, are selected by two windows of length T_c, one starting at time t_1 and the other at time t_2. Both data portions are then normalized to the same energy, and their mean values are set to zero (DC offset elimination). The coarse delay between the two windows is $T_c = t_2 - t_1$. The maximum of the cross-correlation gives the fine delay, T_f. Thus the exact time delay between the two echoes is given by

$$T = T_c + T_f$$

where the value of T_f can be either positive or negative. This procedure does not require knowledge of the initial time, or determination of the exact arrival time of each echo. It uses the whole shape of the wavefront signals, and therefore diminishes the effect of local uncorrelated.

3. 2.2 Experimental determination of phase velocities

Usually the conventional pulse-echo technology is not suitable for phase velocity measurement. Thanks to the special geometry in the circumferential problem and our novel technology, we have developed two methods for the phase velocity measurement.

a) Pseudo-standing wave method

In this method long duration tone-burst pulses, or pseudo-CW input signal, were used. Because of the special property of the circumferential wave which propagates round

52

and round along the circumference, standing waves can easily be formed in the output signals when the duration of the tone-burst input is long enough, *e.g.* covering more than one circumference period. By measuring the adjacent frequencies f_n and f_{n+1}, where the signals are at maximum or minimum (constructive or destructive interference), the phase velocity can be estimated by $V = 2\pi R \cdot (f_{n+1} - f_n)$. Thus the phase velocity values can be measured at certain discrete frequencies. Since in our case Δf was typically in the order of 10^{-2} MHz, the dispersion effect on the accuracy of the integration constant should not be significant if a phase velocity value is at a frequency where the dispersion curve does not have a sharp slope.

b) Integration method

In principle, the phase velocity dispersion curve can be derived by integrating the group velocity curve. The latter can be experimentally obtained from the time delay measurement. This requires sufficient group velocity data points measured at different frequencies. Although the principle seems obvious, the detailed procedure is not trivial. It is worth giving a brief derivation here.

By definition, we have

$$v_g(\omega) = \frac{d\omega}{dk} \tag{3.2.1}$$

$$v_p(\omega) = \frac{\omega}{k} \tag{3.2.2}$$

or

$$v_g(f) = 2\pi \frac{df}{dk} \tag{3.2.3}$$

$$v_p(f) = \frac{2\pi f}{k} \tag{3.2.4}$$

53

From (3), we have

$$dk = 2\pi \frac{df}{v_g(f)} \tag{3.2.5}$$

Integrating (5) gives

$$k = 2\pi \int \frac{df}{v_g(f)} + k_0$$

$$= \frac{1}{R} \int T_g(f)df + k_0 \tag{3.2.6}$$

where k_0 is an integration constant and

$$T_g(f) = \frac{2\pi R}{v_g(f)}$$

is the group time delay over the circumference at frequency f.

Substituting (6) in (4) yields

$$v_p(f) = \frac{2\pi f}{\frac{1}{R} \int T_g(f)df + k_0} \tag{3.2.7}$$

The group time delay $T_g(f)$ can be experimentally measured, and the integration constant

$$C = \frac{2\pi f_0}{v_p(f_0)} - K(f_0) \tag{3.2.8}$$

is to be determined, where $K(f) = \left[\frac{1}{R} \int T_g(f)df \right]_{f=f_0}$

Thus, in order to obtain the phase velocity dispersion curve $v_p(f)$, we need integratable $T_g(f)$ data points, i.e. a smooth $T_g(f)$ curve, as well as a known value of v_p at a frequency f_0 at which the value of $\left[\int T_g(f)df \right]_{f=f_0}$ is also available.

54

In this work, a sufficiently smooth experimental $T_g(f)$ curve over a wide frequency range was obtained by employing the chirp IDT configuration. Integration constant $v_p(f_0)$ values were also experimentally measured at 2 MHz and 5.4 MHz, respectively, by using the pseudo-standing wave method described in a) with a uniform IDT transducer.

3.3 MEASUREMENT PROCEDURES

3.31 Signal generating and receiving systems

A Ritech Ram 10000 system was used at Concordia for delay time measurement, using the integrated and contact transduction methods. Fig. 3.3.1 shows such a system and the measurement arrangement. High power tone-burst signals, *i.e.*, square-pulse modulated envelopes at a specific frequency with a narrow bandwidth were generated and applied to the transducer. With this technique the response of the transducer can be controlled by the signal generator. By varying the output frequency of the tone-bursts within the bandwidth of the transducer, acoustic signals at different specified frequencies can be obtained. This method is very useful for directly measuring the time delay at a given frequency, especially for broadband transducers.

A conventional pulser-receiver system was used at IMI, NRC for measurements using the combined contact and laser probe methods. The system output a pulse which was Gaussian-like and broadband. The response of the transducer depends on the properties of the transducer. In this case, if the transducer is a broadband one, frequency filters are needed to precisely determine the delays at specific frequencies. The advantage

of the single pulse method is that, with a broadband transducer and with the help of narrowband filters such as provided with LabVIEW, time delay data at different frequencies over the bandwidth of the transducer can be obtained from one measurement. This method is also useful to characterize the response of a transducer.
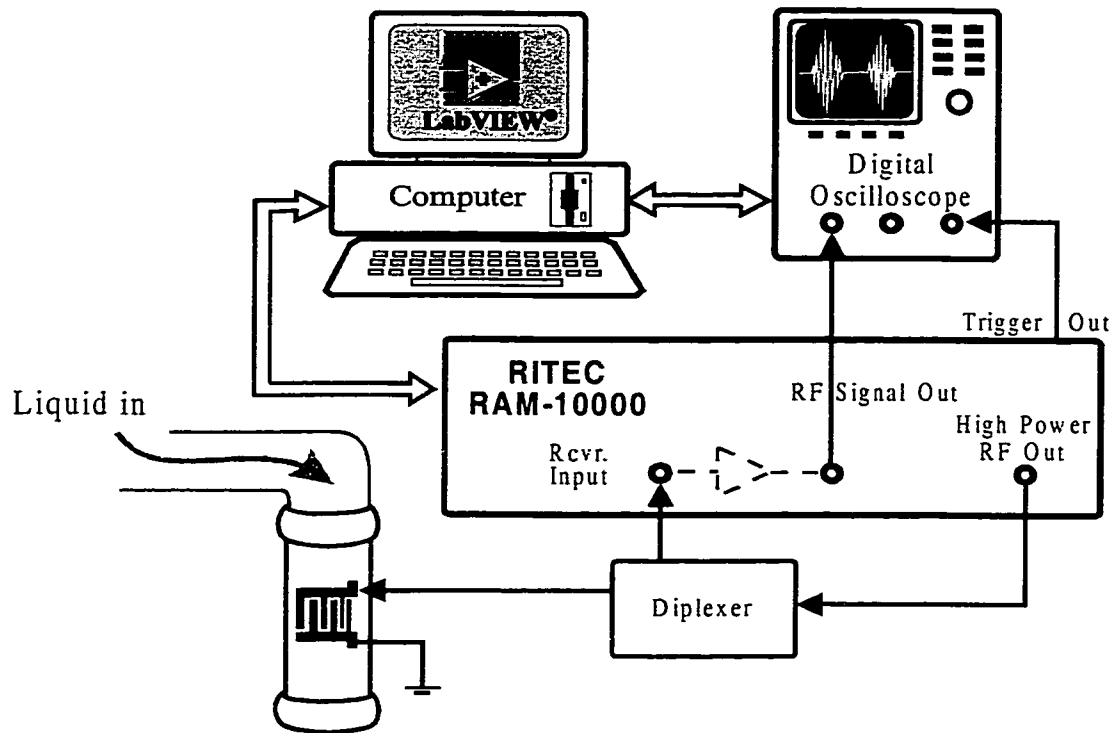
Fig. 3.5. Time delay measurement arrangement

3.3.2 Data Acquisition

a) A digital oscilloscope was used at Concordia and the waveforms were averaged by the oscilloscope to suppress the noise. The digitized data were acquired through a GPIB to a PC with LabVIEW$^®$ programs.

b) At IMI an analog oscilloscope was used and the waveforms were sampled and acquired real-time through a high-speed DAQ card to the computer with LabVIEW$^®$. The averaging was also performed real-time directly on the computer with LabVIEW$^®$.

3.3.3 Data processing and analysis

The following data processing was carried out with LabVIEW$^®$.

a) Frequency filtering

In order to filter out the undesirable signals and precisely determine the time delay values at a given frequency, frequency filtering was performed with LabVIEW$^®$'s virtual filters which could work at any frequency with any possible bandwidth.

Fig.3.6 shows an example of the measured waveforms before and after the filtering. A clear and regular echo train was obtained after the processing.

b) Cross-correlation

Cross-correlation as described in 3.2 was carried on the received echo trains with a LabVIEW$^®$ program. When a window for the first echo was defined with a pair of cursors and a starting cursor was set for the 2nd echo, a window for the 2nd echo was

automatically defined. The software output instantly the time delay value between the selected echoes.

c) Fast Fourier Transform (FFT)

The frequency response of the integrated tube devices was obtained by performing the FFT on the waveforms measured in time domain, again, with LabVIEW$^®$.
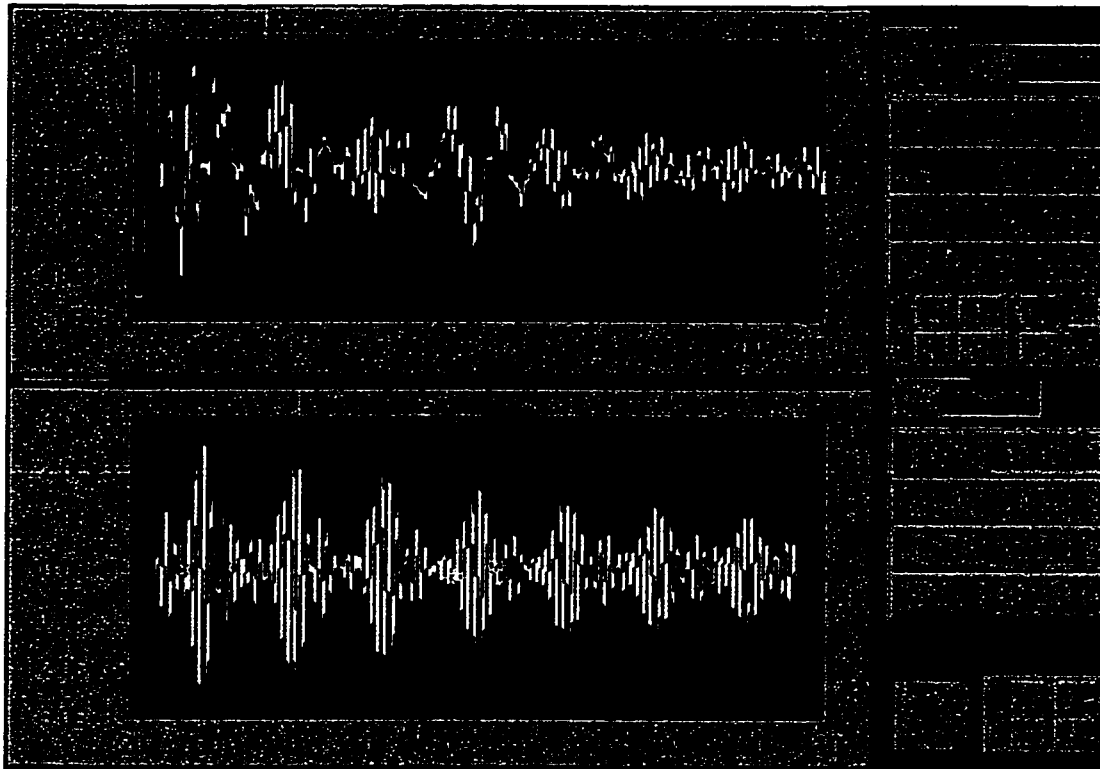
Fig. 3.6   Waveforms measured on an empty stainless steel tube with a thin-disk transducer. The upper one was directly acquired from the oscilloscope and the lower one was filtered with LabVIEW$^®$ at 1 MHz with a bandwidth of 0.1 MHz.

The main reason not to use a network analyzer to measure the frequency response directly was that our devices made for the time delay measurement were of the one-port configuration only. As discussed previously, interference would easily occur for continuos circumferential waves. Secondly, the strong EM feedthrough was very difficult to be eliminated with the structure used, which gave much higher signal level than the acoustical signal.

The FFT was made on the second echo in the received echo trains, which was totally uncoupled from the EM signals. To obtain a full spectrum, tone-bursts with the widest passband available on the Ritech system were applied without a pre-filtering.

CHAPTER 4. EXPERIMENTAL RESULTS AND DISCUSSION

4.1 DISPERSION CURVES IN EMPTY AND WATER-FILLED TUBES

4.1.1 Empty stainless steel tube

Dispersion curve measurements were carried out on a stainless steel tube with a wall thickness of 0.254 mm and an outer diameter of 9.8 mm. This tube was coated with thin PZT film, and with a combined chirp IDT pair on its outer surface, the same device characterised in the previous chapter (Fig. 3.6 (b)). High power tone-bursts at different frequencies were applied on the IDTs, with steps of 0.05 MHz. The frequency range was between 0.8 MHz and 6.6 MHz, i.e. the frequency-thickness product $f \cdot d = 0.2$ MHz $\cdot$ mm to 1.7 MHz $\cdot$ mm, which covered the most sensitive $f \cdot d$ range of the lowest flexural modes. The signals measured at each frequency were carefully processed, and the time interval was precisely determined using the cross-correlation method. Typical received echo trains are presented in Fig. 4.1, all of which show a very good signal-to-noise ratio. It is clearly seen that the time interval of the echo train varies systematically with the frequency. At frequencies lower than 3 MHz, signals of a single mode were obtained, which was identified as the A_0 mode. In the frequency region between 4 MHz and 6 MHz, two modes were found in the echo trains, the second being identified as the S_0 mode. The amplitude difference between the two modes was about 10 to 15 dB. The A_0 mode was dominant over the whole accessible frequency range.
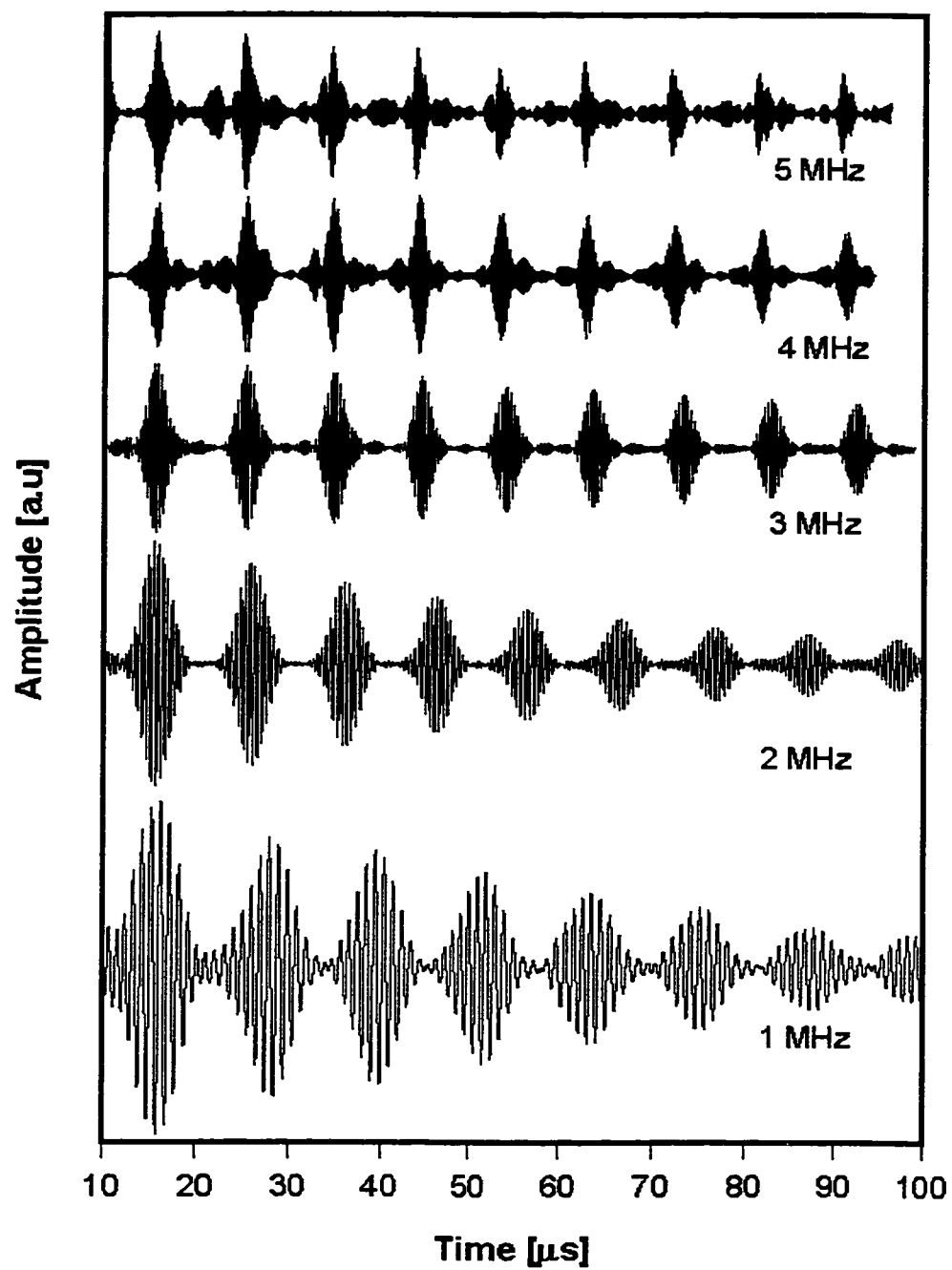
Fig. 4.1 Received echo trains at different frequencies for an empty stainless steel tube, measured with a chirp IDT.

The results obtained with a uniform IDT on an identical stainless steel tube showed some difference: at frequencies around 2Mhz, only the A_0 mode was generated, while near 5.4 MHz, S_0 mode was uniquely observed. The first two peaks in Fig. 3.7 (a) correspond to the two modes at their center frequencies, respectively. Around 4 MHz, both modes were observed. At about 8.3 MHz, a very weak echo train was observed. The group velocity values showed that this was the A_1 mode.

By re-plotting the theoretical dispersion curves with wavelength vs. frequency, as shown in Fig. 4.2, we can have a clear picture as to how these three lowest Lamb-type modes are generated (and detected) by the chirp IDT and/or the uniform IDT. As described previously in Chap. 3.3.1, the wavelength λ of the signals generated (and detected) by an IDT has approximately the same value as the IDT finger spacing P, with a certain bandwidth depending on the detailed IDT structure.

The constant finger spacing value of the uniform IDT intersects with the wavelength curves of all the three modes, at three well separated frequencies with very narrow frequency bands.

For the chirp IDT, the varied finger spacing range covers the three modes over three frequency bands, each of which has wide overlaps with the others.

Fig. 4.3 shows the frequency characteristics of a uniform IDT and a combined chirp IDT pair, respectively, made on two identical stainless steel tubes. The frequency responses were obtained from the time domain measurement by performing the FFT with LabVIEW®.
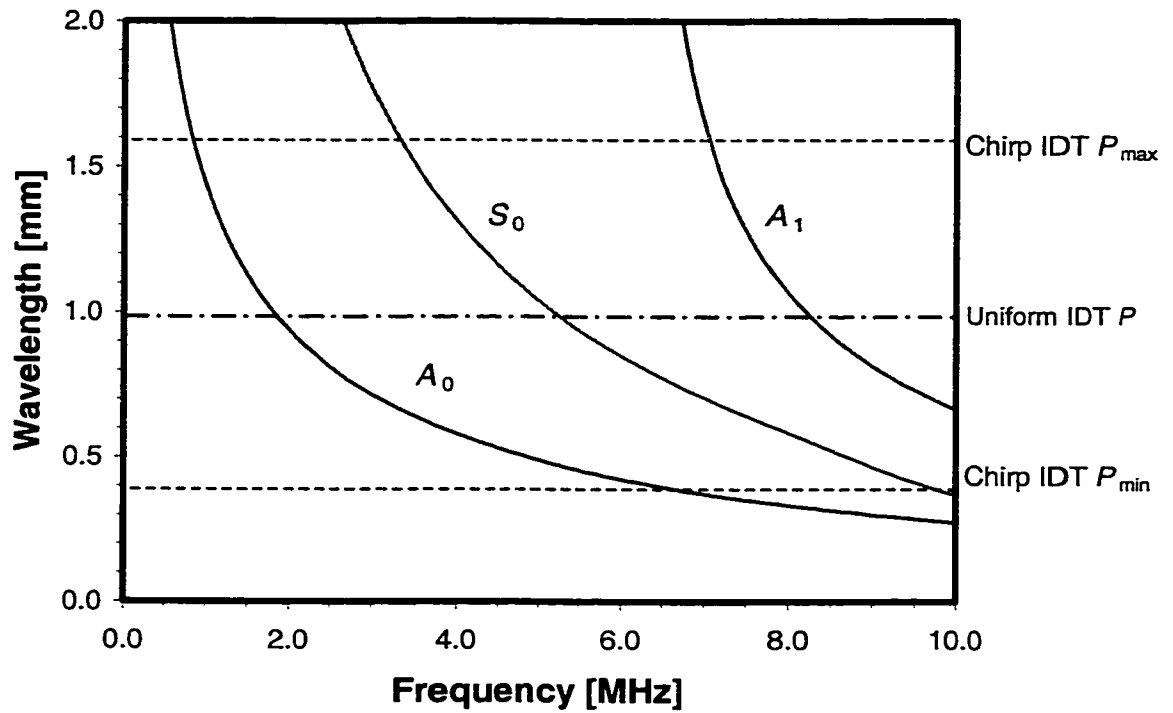
Fig. 4.2 Relation between wavelength of the Lamb-type modes and the finger period P of the IDTs on the stainless steel tube sample.

Three narrow band peaks corresponding to the first three Lamb-type modes were found in the frequency respond of the uniform IDT. At the center frequency of each peak, the uniform IDT period has an intersection with the wavelength curve of the corresponding mode, as seen in Fig. 4. 2 .
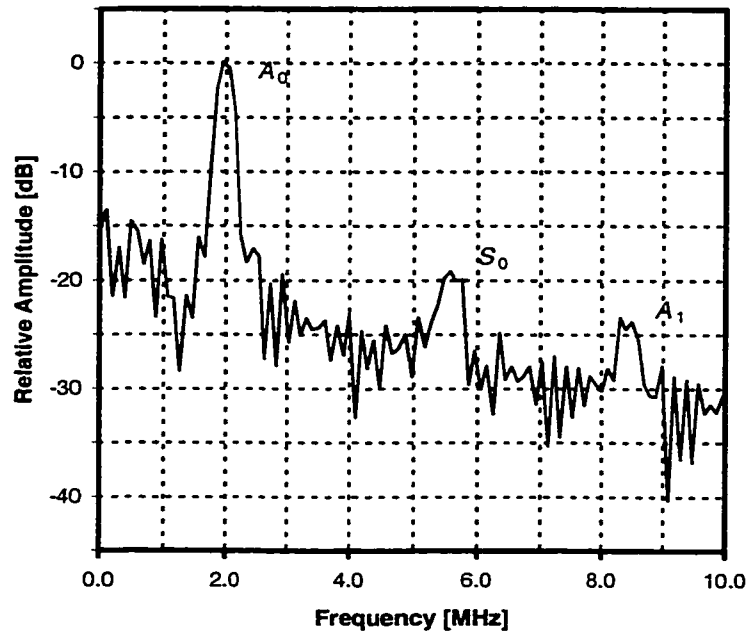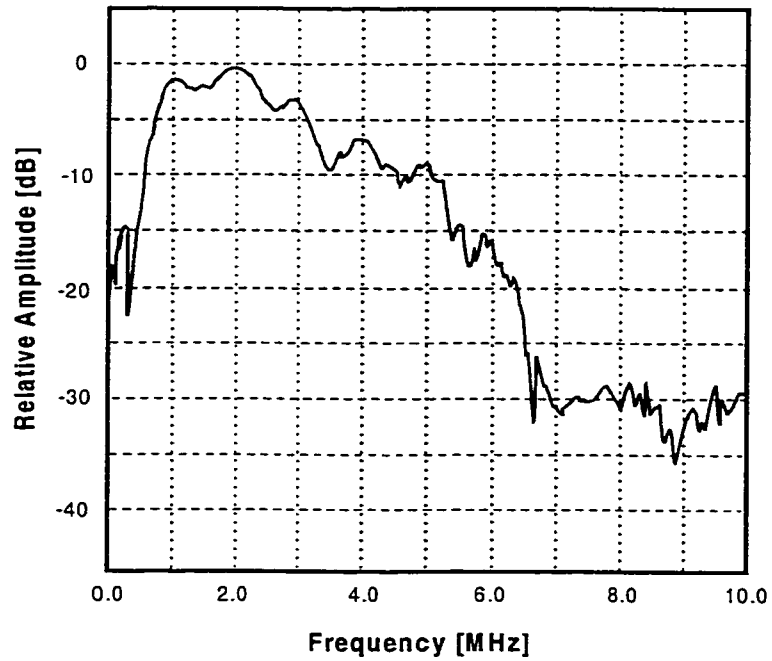
Fig. 4.3 Frequency response obtained by FFT of the received signals on (a) a uniform IDT and (b) a chirp IDT pair made on two identical stainless steel tubes coated with PZT film, respectively.

On the other hand, the broadband characteristic of the chirp IDT is very well shown in Fig. 4.3 (b). The frequency bandwidth (BW) of the transducer is extremely wide, with $BW_{(5\ dB)} \approx 2.5$ MHz, $BW_{(10\ dB)} \approx 4.5$ MHz, and $BW_{(20\ dB)} \approx 6$ MHz, respectively.

The three possible mode are coupled, but there is no doubt that the total contribution is mainly from the A_0 mode.

The group delay time for the A_0 mode was easily derived from the well defined interval in the echo trains as shown in Fig. 4.1.

Because they were much less effectively excited and were emerged by the dominant A_0, in the whole accessible frequency range, the S_0 mode was quite difficult to be separated from the echo train and the A_1 mode was not seen at all with the chirp IDT. With extremely careful processing, we eventually picked up the S_0 signals from the echo trains.

The group velocity and phase velocity dispersion curves, both derived from the delay time measurement, are shown in Figs. 4.3 and Fig. 4.4, respectively. They are plotted together with the theoretical curves for comparison.

The experimental phase velocity curve was obtained by numerically integrating the measured time delay data over the frequency. The integration constants for the A_0 and S_0 curves were determined by applying the pseudo-standing wave method on an identical tube with a uniform IDT at frequencies 1.98 MHz and 5.38 MHz , respectively.

Both the experimental V_g and V_p curves are in very good agreement with the theoretical modelling for the empty tube. Data points measured with other methods on an identical tube sample at several discrete frequencies are also included in the figure.

The excellent agreement among the data obtained from all three different approaches verifies that the measured dispersion is real, not just an artificial effect of the "dispersive" chirp IDT itself.
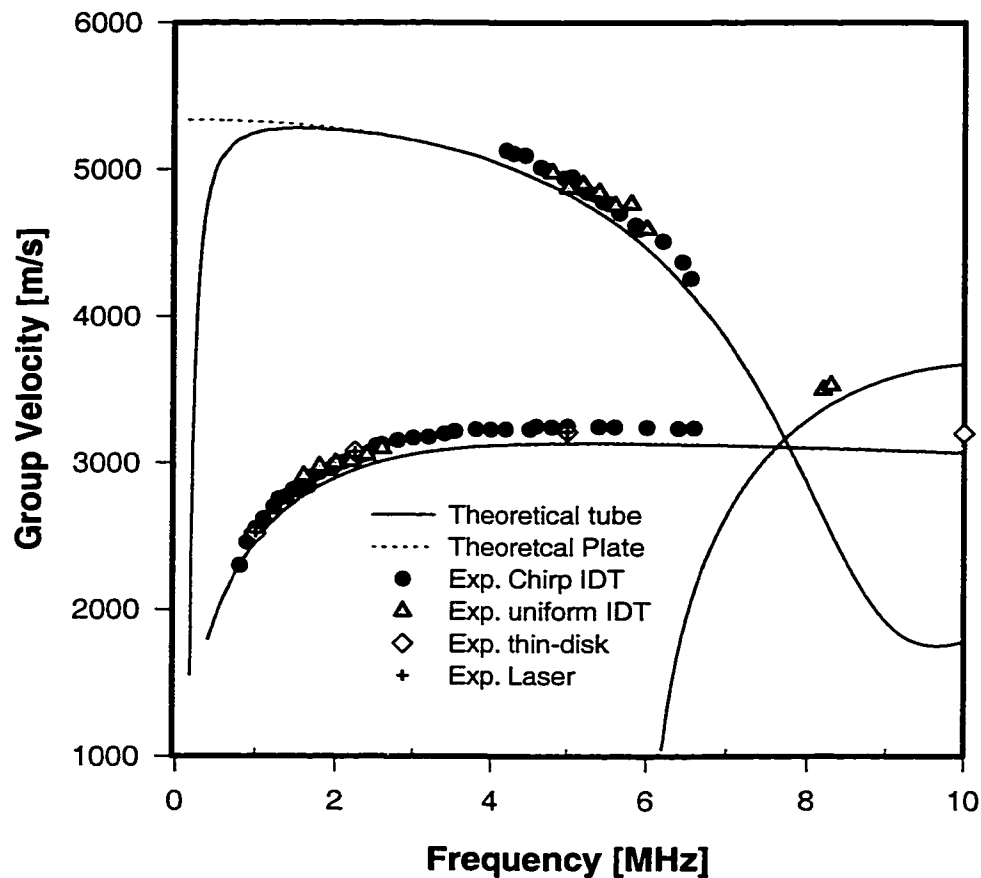

Fig. 4.4(a) Measured group velocity dispersion curves of the circumferential waves for an empty stainless steel tube by different approaches, with a comparison to the theoretical results.
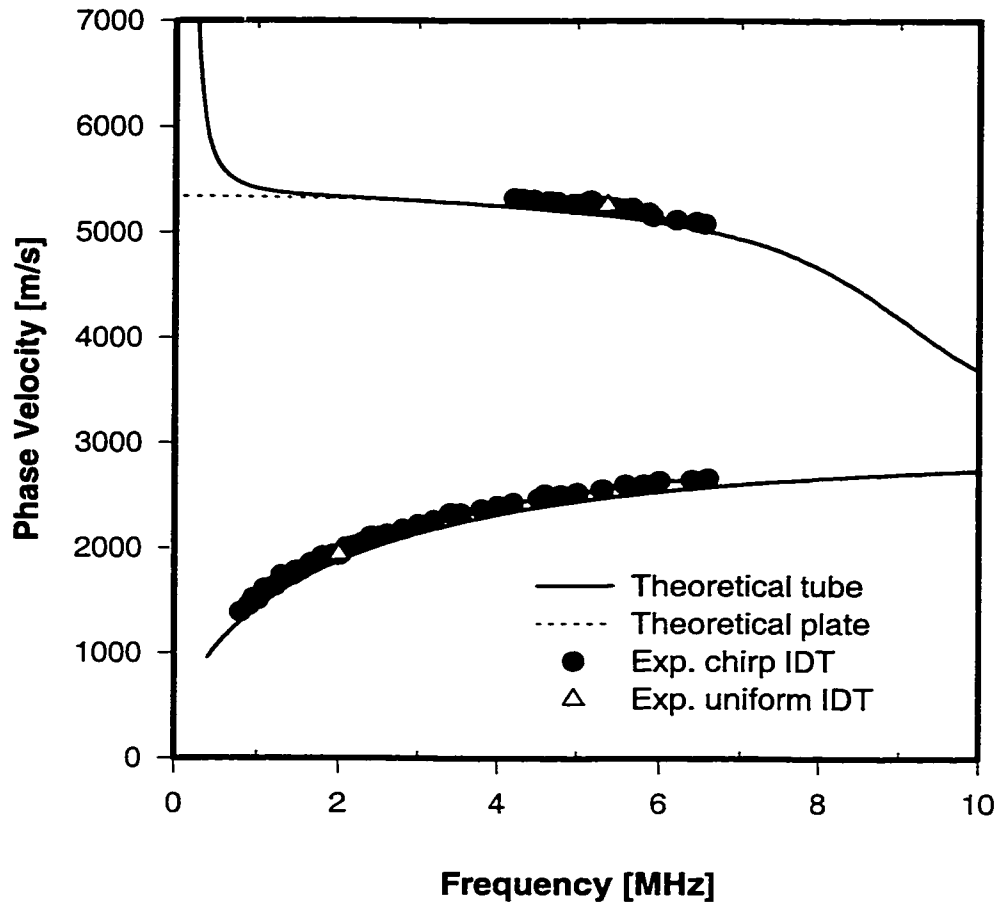
Fig. 4.4(b) Experimental phase velocity dispersion curves of the circumferential waves for an empty stainless steel tube, with a comparison to the theoretical results.

4.1.2 Water-filled stainless steel tube

When the same stainless steel tube was filled with water, signals were detectable between 0.8 MHz and 2.4 MHz, at which frequency range only the A_0 mode was measured in the empty tube. Representative echo trains and the measured time delay intervals to compare these two cases are shown in Figs. 4.5 and Fig 4.6, respectively. It is obvious that the time intervals in the water-filled tube are significantly larger, especially on the high frequency side.

In general two mechanisms are possible for this large change in time delay:

(i) The waves are severely leaky. Unlike the water-loaded plate case, due to the curvature the leaked waves may re-enter the tube wall under certain conditions, and be emitted again, and may be received by the transducer after several reflections. In this case the waves would travel mainly in water, which propagate in very much the same wave as the "Whisper Gallery" modes.

(ii) The flexural motion in the tube is strongly modified when it is filled with water. The observed signals are either from the modified A_0 mode present in the tube only, or from new circumferential modes associated with the flexural motion in a compound tube-water system.

Consider first the leaky case. In order for the signals to be received by the transducer, the path of the leaked and reflected waves should form nearly a closed loop, assumed to be equilaterally polygonal. Since the sound velocity in water $V_g = V_p = 1.48$ Km/s, and typically the measured time interval $\Delta T = 13.1$ us, the total distance the waves could have traveled in water is estimated to be 19.3 mm, which is approximately twice of the tube diameter (2 x 9.8 = 19.6 mm). Thus only the path directly across the diameter of
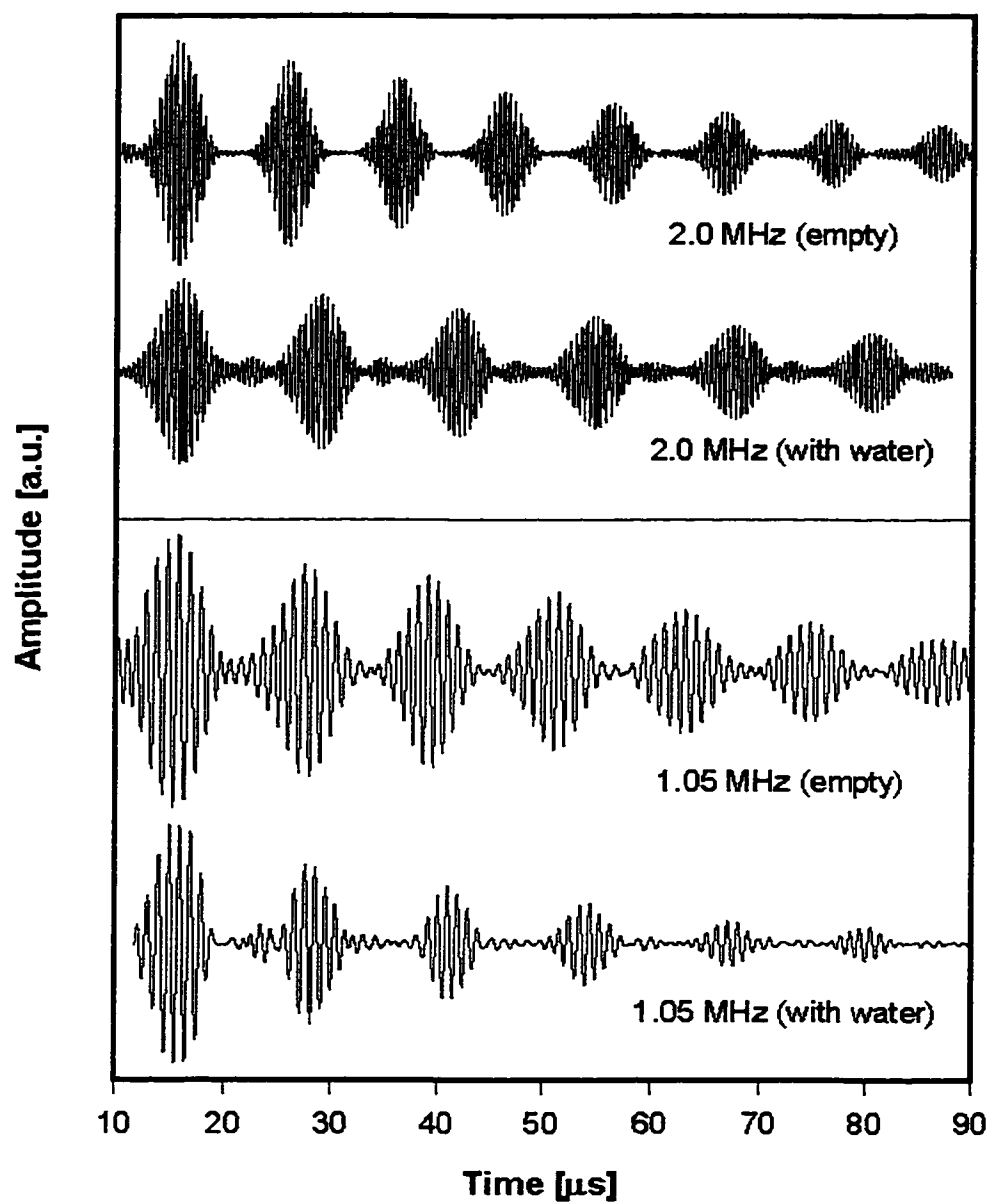
Fig. 4.5 Received time delay signals for an empty and water-filled stainless steel tube at different frequencies.
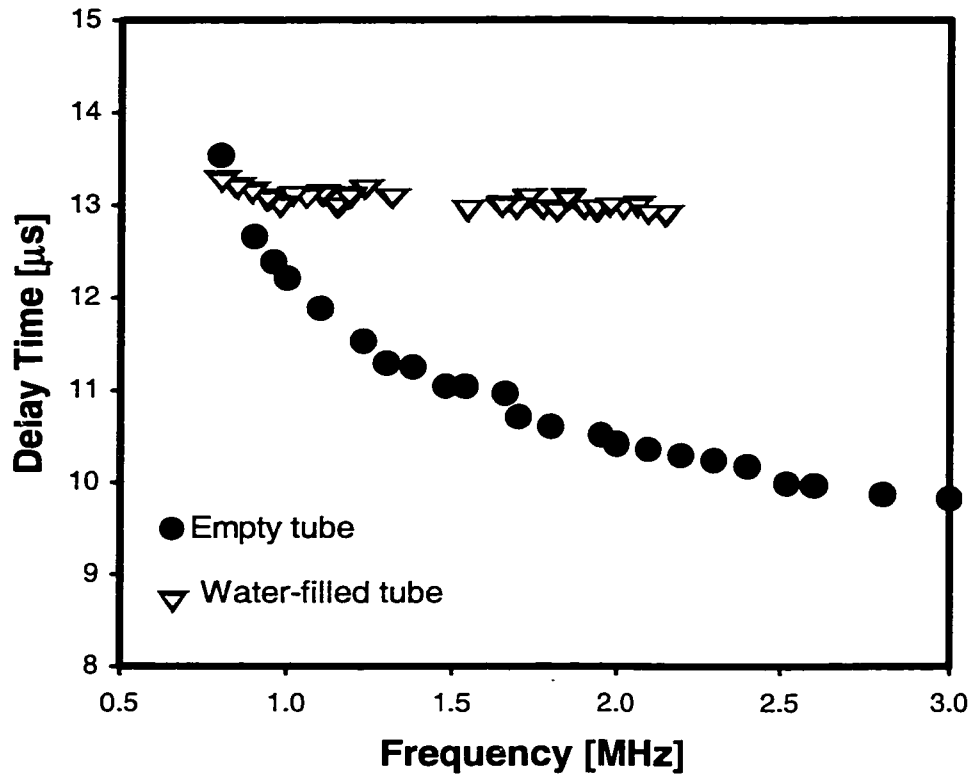
Fig 4.6 Comparison of the measured time delay intervals for an empty and water-filled stainless steel tube.

the tube is possible. Any other polygonal paths (triangle, square, pentagon, etc.) defined by the circle of $R \approx 4.9$ mm would lead to a much longer delay time, and are therefore excluded.

To evaluate this hypothesis, the following experiments were performed:

(1) Insert co-axially an empty tube with an outer radius close to the inner radius of the water-filled tube device, which would have profoundly modified, delayed or smeared out any existing bulk wave in the water. No change in either the delay time or amplitude of the echoes was observed.

(2)Touch the *outer surface* of the tube at arbitrary positions with a wet Q-tip. The signal amplitude decreases significantly.

(3) Fill the tube with different water levels parallel to the tube axis. The time delay increased systematically as the level increased, but the amplitude showed little change for different levels.

(4) Perform the measurement using the combined contact and non-contact methods on an identical stainless steel tube, with the laser probing point well off the opposite position of the generating transducer. The measured time intervals were the same as obtained by the IDT, although the signal-to-noise ratio was obviously poorer. The comparison of the measured echo trains is given in Fig. 4.7. The paired echoes with the same time interval in the echo train received by the laser probe also strongly support the notion that the received signals were circumferential.

All of the above experimental evidences rule out the leaky wave assumption. We thus conclude that in the water-filled stainless steel tube the received signals were from the acoustic waves traveling in the tube wall around the circumference. The observed large change in the time delay is not trivial, but reflects a significant change in the group velocity of the circumferential waves.
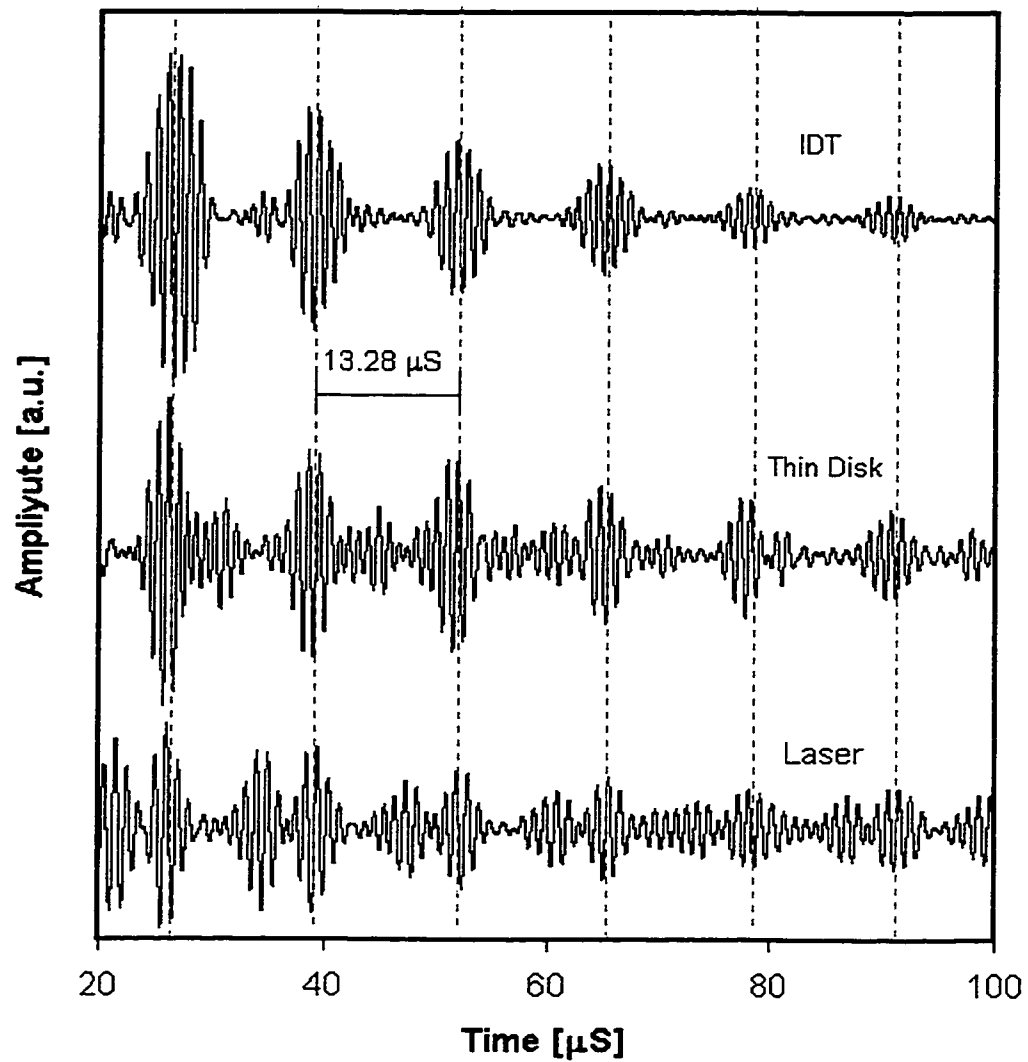
Fig. 4.7. Comparison of the acoustical signals measured in stainless steel tubes of the same size filled with water, by three different configurations at 1 MHz.

Having established that the observed signals are circumferential, we can now derive the group velocity directly from the measured time intervals, and compare the results with our theoretical curves for the water-filled tube. The comparison is made in Fig. 4.8. In the water-filled case, no sufficiently clear resonance was observed with the pseudo-standing wave method, and therefore the experimental phase velocity curve was not available by the integration method without an experimental integration constant.

In Fig. 4.8, it is obvious that the measured V_g curve, with nearly a constant value about 2380 m/sec at frequencies around 1 MHz and 2 MHz, respectively, has no similarity with that of the A_0 curve, except that at the lowest frequency ($\sim$0.8 MHz) there is an overlap. On the other hand, the data points are very close to the "plateau" formed by the maximum V_g of the W modes. Unfortunately, this is just a coincidence. The possibility that we have observed the W modes are immediately excluded by noting that any of the maximum V_g of the W modes occurs at the cut-off frequency where the phase velocity goes to infinity, and so does the wavelength. In our case only waves with finite wavelengths close to the finger spacing of the IDT are excitable and detectable. Furthermore, the W modes at their cut-off frequencies propagate in the water cross the tube diameter, which we have just excluded by a series of experiments.

Our theoretical modeling is not sufficient to interpret the circumferential modes observed.

Although there have been many theoretical studies and several experimental reports on circumferential elastic waves in cylindrical shells immersed in a liquid, no reported theoretical results can be used to interpret our observation, and so far no reported experimental results are similar to ours.

It is commonly accepted in theory that flexural motions could exit (at least mathematically) in the liquid-loaded cylindrical shells, with an A mode, which is subsonic, in the low $f \cdot d$ (frequency-thickness product) region, and an A_0 mode, which is supersonic, in the mid $f \cdot d$ region. The A mode is also called the Scholte-Stonely mode, which propagate only at the water-solid interface, and most of the acoustic energy is in the liquid. The A_0 mode propagate in the shell but is strongly leaky and practically could not survive in the liquid-loaded cylindrical shells.

Talmant et al. [24-26] irradiated thin cylindrical shells immersed in water with short acoustic pulses, and measured group velocities of waves circumnavigating the cylinder. A "fast" wave was identified with S_0, and a "slow" wave with a Scholte interface wave A. The A_0 mode was not observed, the reason being given that radiation damping is much stronger for this mode. A third weak circumferential mode with a group velocity $V_g = 2450$ m/sec was observed but not identified. Izbicki et al. [27-29] used a different geometry, where the transducer was placed on the inner wall of an empty cylindrical shell, and the receiving transducer was placed in the liquid outside of the tube. The results were compatible with those of Talment et al. for external excitation; S_0 and A modes were observed but no A_0 mode was identified.

By the nature of the configuration in our work, where a chirp IDT is placed on the outer surface of the water filled tube, we are only able to detect tube-borne waves such as A_0 or S_0 modes, and not the Scholte-Stoneley waves at the solid-fluid interface inside the tube.

Since in the frequency region $f \cdot d \approx 1$ only A_0 mode was excited for the empty tube with the given IDT, the observed waves in the water-filled tube should be related to

the flexural vibration of the tube. Furthermore, it is intuitively obvious that the flexural waves can be strongly influenced by the liquid filler, which would lead to a significant change in the propagation velocity, while the Lamb-type symmetric S_0 waves are not very sensitive to the presence of a liquid filler.

Very recently, as this thesis was being finalized, Veksler *et al.* [55] and Maze [56], in response to our short communication to JASA [54], presented to us their latest theoretical results, in which a new family of modes are predicted in liquid filled cylindrical shells.

Veksler *et al* found that, between each two non-zero order Whispering Gallery modes, WG_l and WG_{l+1}, there exisits the l-th order of the so called "S-shaped Whispering Gallery" mode, SWG_l. Fig. 4.9 illustrates the phase velocity dispersion of these modes in a liquid-shell-liquid configuration. The plot is schematic, and the original curves provided in the private communication are not directly quoted here. It is seen that the l-th non-zero order mode is confined by the WG_l and WG_{l+1} modes, with the SW_0 confined by the A_0 and WG_1. On the low frequency side it approaches the WG_l while at the high frequency side it approaches WG_{l+l}, forming an S-shaped curve across the A (or A_0) mode

According to Veksler *et al.*, while the A (or A_0) waves and the WG waves exist in two subsystems - the shell and the liquid filler, respectively, the SWG waves belong to the compound liquid-filled tube system. *The flexural motion of the shell is realized in the form of the SWG waves.*

Maze performed a particular computation for a water-filled stainless steel tube similar to our experimental sample, using material parameters slightly different from

ours. He also obtained modes corresponding to the SWG family, which he named WT modes. The results are schematically plotted in Fig. 4.10 with our experimental V_g data, the original curves provided in the private communication not being directly quoted. For comparison all the units and scales in Maze's curves have been converted. We observe that the group velocity of the WT_1 (or SWG_0 by Veksler) mode has a maximum near 1 MHz and that of the WT_2 (or SWG_1) mode has a maximum near 2 MHz. These two maximums, valued about 2380 m/s, coincide with the two "plateaus" in our experiment curve. By examining Maze's V_p curves in Fig. 4.10 (a), we see that the WT_1 mode is very close to the A_0 mode at low frequency (f < 1 MHz) and the WT_2 mode has an intersection with the A_0 mode near 2 MHz, around which the two curves are also very close. That means that in the frequency regions around the two peaks in the group velocity of WT_1 and WT_2 modes, the two WT modes have a strong interaction with the A_0 mode.

If we ignore the difference in values and the detailed dispersion trends, our experiment observation was so far best interpreted theoretically by the WT (or SWG) modes.

Both Veksler *et al* and Maze made their computations base on investigating the scattering of an incident plane wave by a liquid-filled cylindrical shell, using the resonance scattering theory. The question followed here is whether the WT (or SWG) modes are generatable and detectable with our experiment configuration. A positive answer can be given with the following argument:

The IDT may initially generate the A_0 waves in the tube, which later become the WT waves due to the strong interaction between the A_0 and the WT_1 and WT_2 at particular frequencies. Once being steadily formed, the WT waves propagate in the
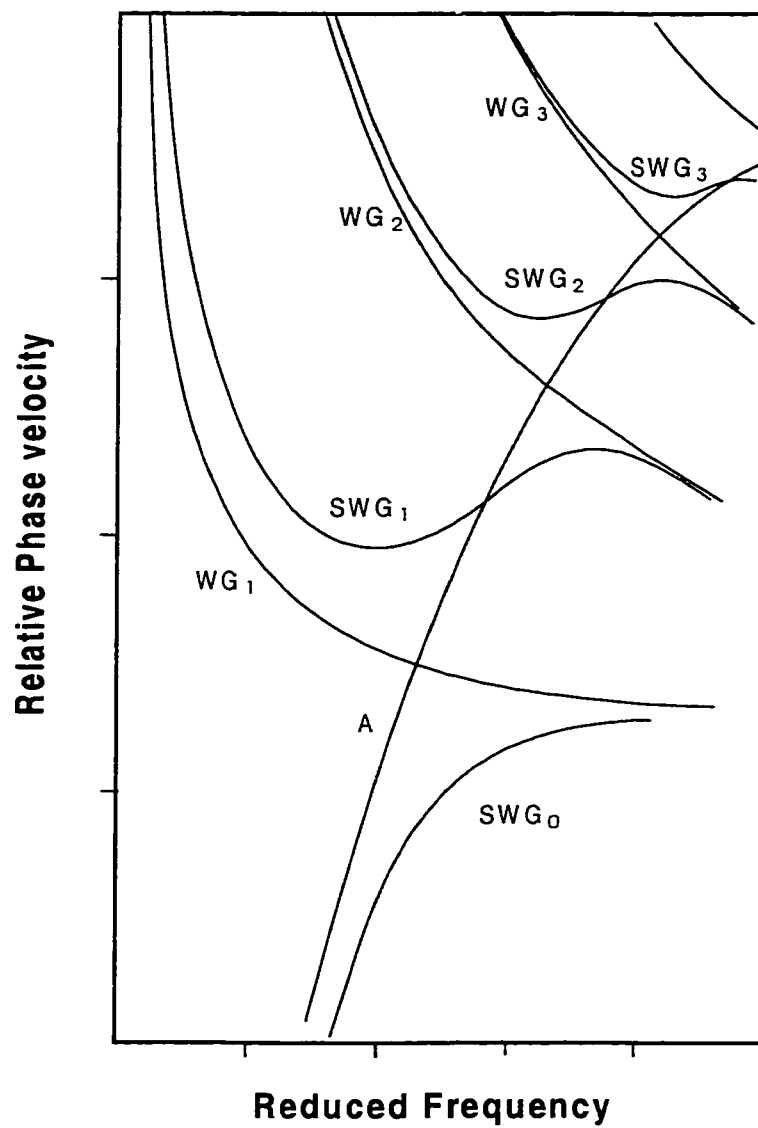
Fig. 4.9 Schematic dispersion curves of the phase velocity for the three different types of circumferential modes in a liquid-filled tube.
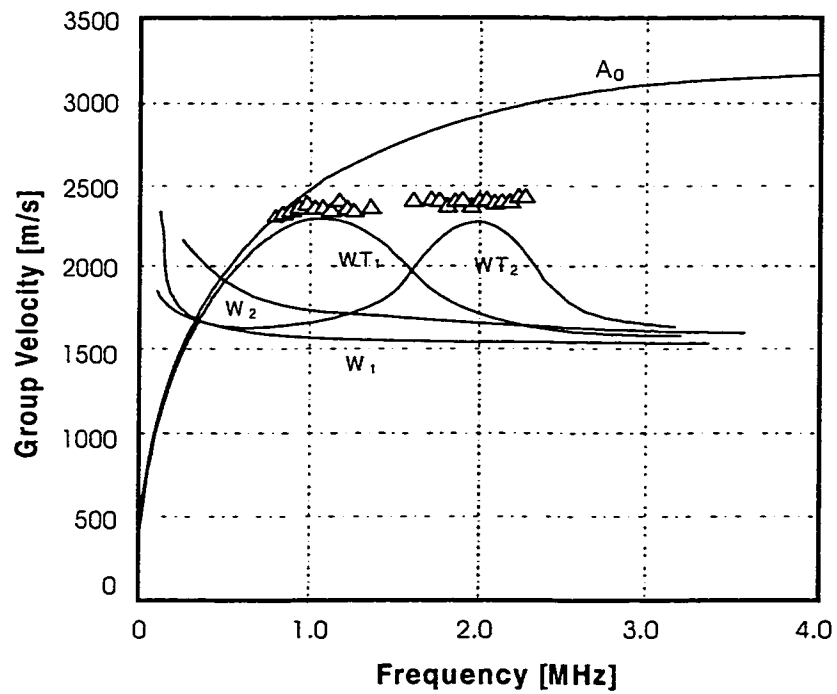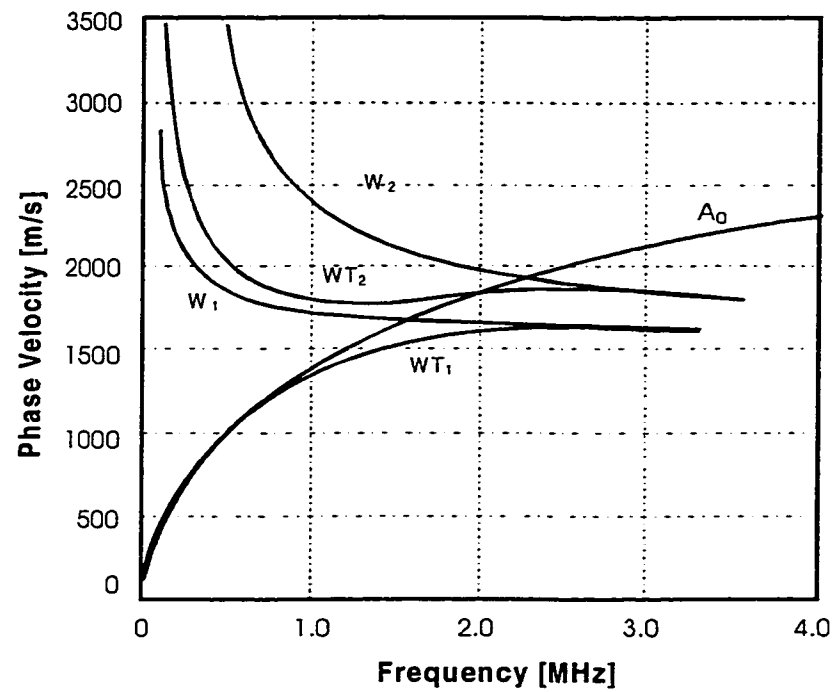
Fig. 4.10   Comparison of the experimental results and the theoretical
dispersion curves in [56] for a water-filled stainless steel tube.

compound water-tube system, and thus may be easily detected repeatedly by the IDT on the tube surface. This could occur only in the frequency region where the A_0 mode and the WT modes had a strong interaction. Around 1.5 MHz, the A_0 mode is well separated from the WT_1 and WT_2 modes, but it strongly interacts with the W_1 mode. If the system is more in favour of the W_1 mode than the A_0 mode, and the acoustic energy is then concentrated in the water column by the nature of the Whispering Gallery modes, the signals could hardly be detected by the IDT on the outer surface of the tube. That may explain the loss of signals in this frequency region. The same reason may apply to the frequency range near 2.4 MHz where the A_0 mode has a strong interaction with the W_2 mode. At higher frequencies the A_0 mode has no interaction with the others but it is highly attenuated and cannot survive in the shell.

The reason we did not detect the signals at frequencies below 0.8 MHz is simply that the wavelengths of both the A_0 and the WT_1 modes are beyond the upper limit of our IDT finger spacing, even though these two modes have the strongest interaction in this frequency region, and they are basically the same at even lower frequencies.

In addition to the difference in values, the main discrepancy is that our experimental curve is more plateau-like than curved peak-like. These discrepancies may be partly due to experimental uncertainty and partly to the parameters used.

4.2. MODE CONVERSION BETWEEN CIRCUMFERENTIAL AND COMPRESSIONAL WAVES.

In the last section we have unambiguously excluded the possibility that the signals received involve strong leakage of the A_0 mode into the water, propagation as a bulk wave in water, and re-conversion to the A_0 mode before the pulse arrived at the transducer. We did, however, observe such phenomenon in a water-filled aluminum shell.

The measurement was made on an aluminum shell with an inner diameter of 91 mm and a thickness of 0.8 mm, using the contact method described in Chapter 3. Tone-bursts at 1 MHz were applied to a piezoelectric transducer of the same nominal frequency. Clear echo trains were obtained both when the shell was empty and when it was fully filled with water. In the empty shell, the echo interval was 93.6 μs, corresponding to a group velocity of 3,081 m/s, which clearly identifies the mode as A_0 (see Fig. 4.11). A delay time of 153.2 μs was found in the water-loaded shell, which is 65% longer than the empty case. Had the propagation been within the shell, the group velocity of the lowest flexural circumferential wave due to the water-loading would have been 1,882 m/sec, which is a huge change from the empty case. On the other hand, if we consider the leakage case which involves mainly bulk waves propagating in the water, the most possible closed path would approximately be an equilateral triangle. This was confirmed by the "blocking" experiment similar to that for the water-filled stainless steel tube. When a cylinder of small diameter was inserted co-axially to the water-loaded chamber, no modification was found in the echo train. When a cylinder of larger diameter was inserted, the echo train was strongly modified. When the diameter of the blocking cylinder was large enough (Fig. 4.12), the echo train was totally killed.

If we assume that the acoustic energy in the vibration generated by the transducer was totally radiated in the water and a pure reflection occurred as the radiated waves hit the shell wall, the most likely closed path for the transducer to receive equal-intervaled echoes is an equilateral triangle in the water, such as that in Fig. 4.12. The total time for the compressional waves in water to complete this path is 160.1 μs, given that the inner diameter of the shell was 91 mm. This is quite a close estimation, but it is still significantly longer than the measured 153.2 μs.
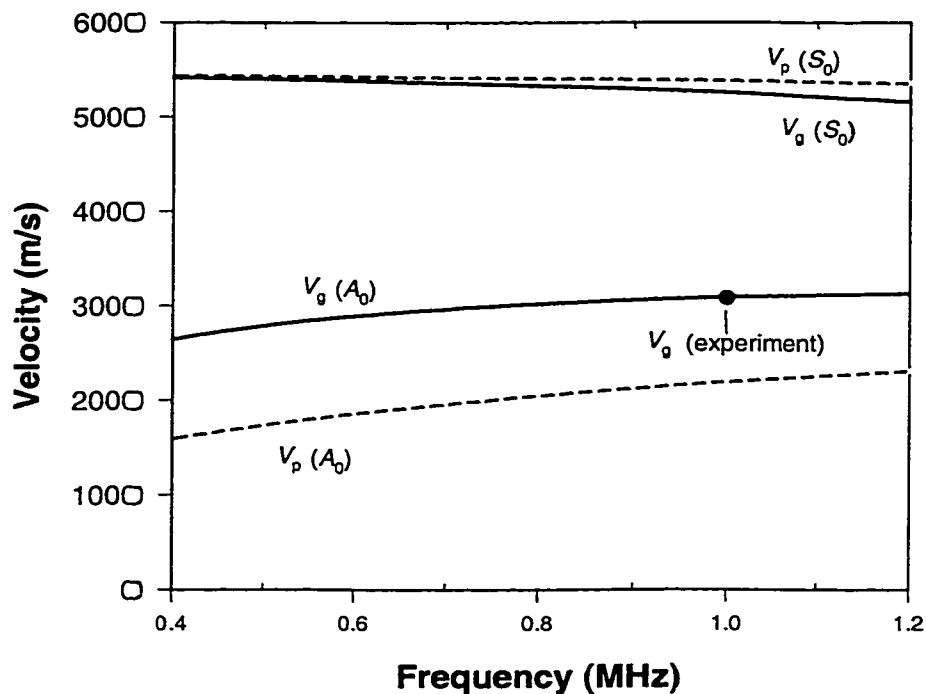

Fig. 4.11 The measured V_g at 1 MHz, and the theoretical V_p and V_g curves for an empty aluminium shell with an inner diameter of 98 mm and a thickness of 0.8 mm.
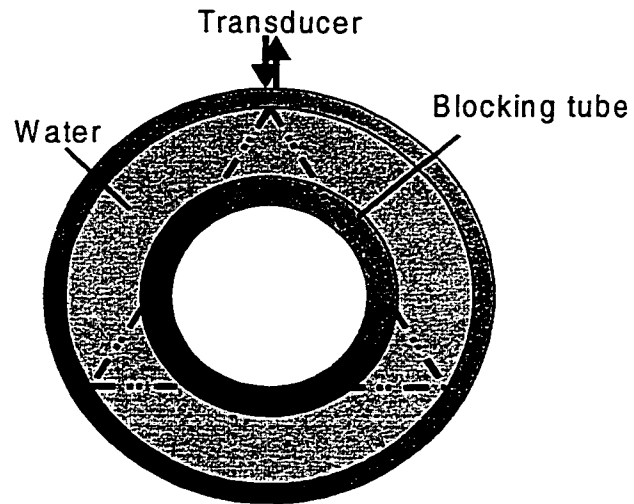
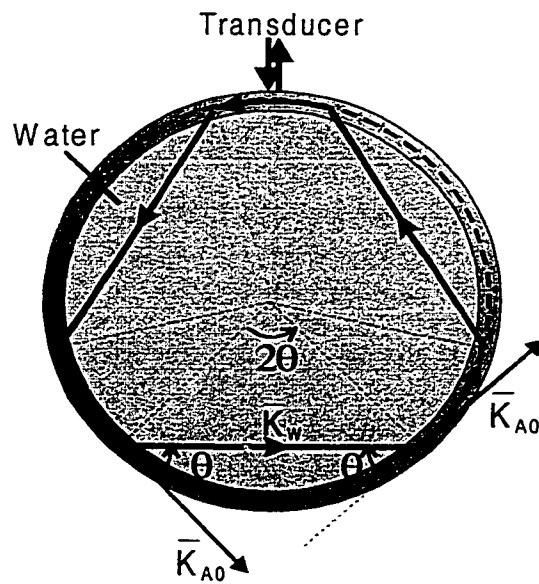**Fig. 4.12   Illustration of blocking the compressional waves in a water-filled shell.**

Fig. 4.13   Illustration of mode conversion between the A_0 wave in the shell and the compressional wave in the water.

A modified picture, such as that in Fig. 4.13, suggests that instead of having totally traveled in water, the waves could have propagated partly in the shell and partly in the water. The path consists of three equal-lengthed straight lines in water and three equal-lengthed arcs along the shell circumference. In this model we assume that initially the circumferential A_0 mode was generated, but strongly leaked into the water with an angle θ. The A_0 waves could then travel in the shell circumference effectively only for a limited distance, such as an arc in Fig. 4.13, before most of the energy was emitted into the water. The resulting compressional waves in the water re-converted into the A_0 mode when they hit the inner surface of the shell. Again, The A_0 mode survived only shortly in the second arc of the same effective length and then emitted back into the water as compressional waves. After another repetition of this procedure the waves finally returned to the starting point. So the total time needed to finish this travel is

$$\tau = \tau_1 + \tau_2 = S / v_g^{A0} + l / c_w \qquad (4.2.1)$$

where $S = R(2\pi - 6\theta)$ is the total length of the three arcs in the shell and $l = 6R \cdot \sin \theta$ is the sum of the three straight lines in the water as shown in Fig. 4.13, v_g^{A0} and c_w are the group velocity of the A_0 mode in the shell and that of the compressional waves in water, respectively. Before we examine whether this assumption is reasonable and find the values of v_g^{A0} in this water-loaded aluminum shell and the emission angle θ of the leaky waves, let us see some very interesting experimental results.

We placed the same aluminum shell horizontally and filled it with water to different levels, as we did with the stainless steel tube for mode identification. Unlike the previous case, where regular echoes were obtained for all water levels, here clear echo trains with equal intervals were observed only at levels near 15 mm and 62 mm, corresponding to ~ 16.7 % and ~ 68.8% of the chamber height, respectively, in addition to the empty (0%) and full (100%) cases. As the water increased or decreased from the four levels mentioned above, the echo trains faded away rapidly. In regions far from these levels, for example 50% of the chamber height, either no significant echoes were observed or they were randomly distributed. Again, in all the partially filled cases the echo trains were either strongly modified or smeared out when blocking tubes were inserted in the water.

We also noticed that there existed a very weak echo in the received signals at around 153~155 μs from the initial triggering time, which is very close to the value of the echo interval in the empty case. This echo, sometimes just above the noise level, was observed for most water levels that were far from being full. This single weak echo and its time location suggests that the A_0 mode in the water-loaded aluminum shell, with a group velocity about the same as in the empty shell, was so strongly attenuated that only the first echo could be weakly detected. It was difficult to precisely cross-correlate this very weak echo with the initial signal, the latter being always coupled strongly with the EM signals. But it is safe to say that the error should not exceed 2 μs by just taking the time reading of the echo at its maximum without a careful cross-correlation. This result is in good agreement with the theoretical calculation that the V_p and V_g of the A_0 mode (if it survives) have very little difference between the empty and water-filled tube.
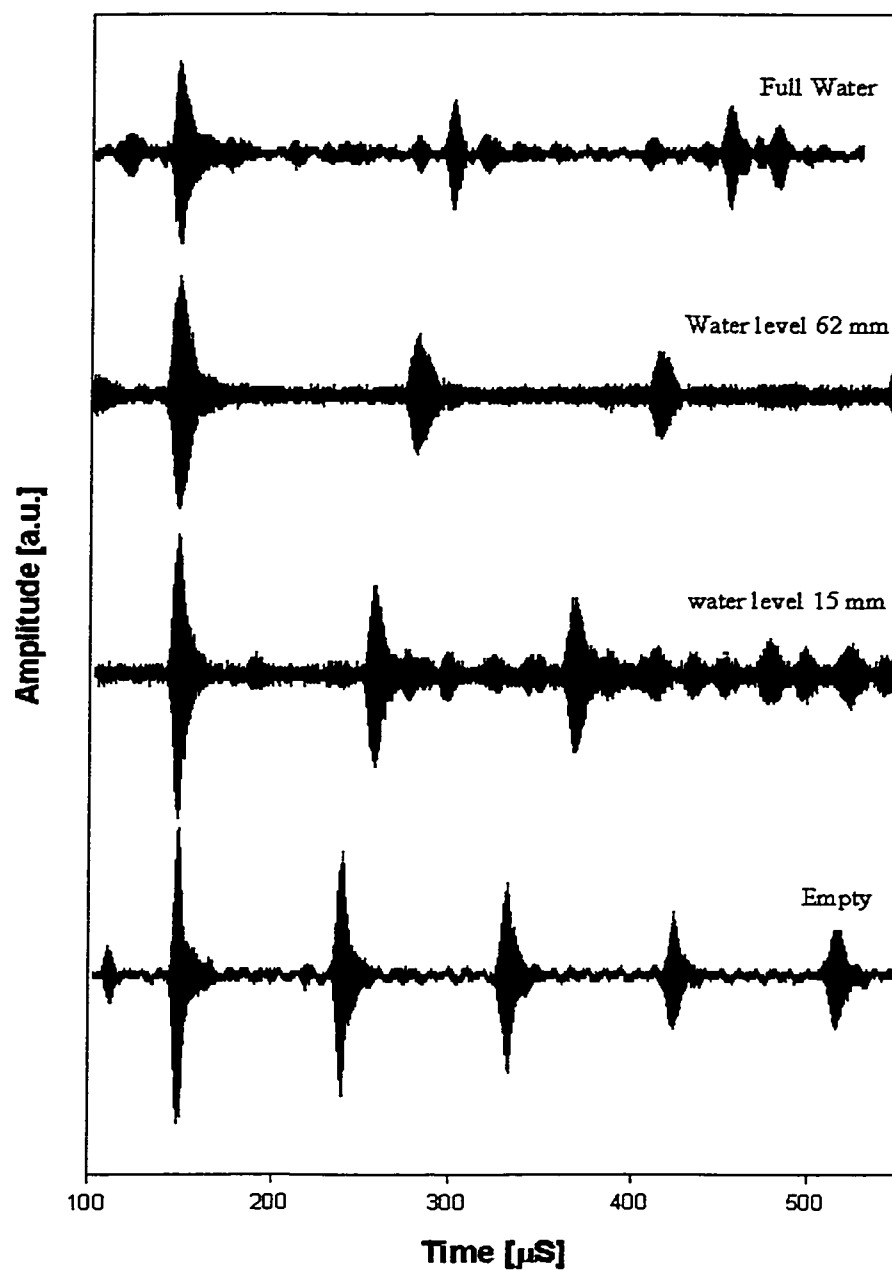
Fig. 4.14 Received echo trains in a horizontally placed aluminum cylindrical shell filled with water to different levels.

Experimental V_p values were not available in this case.

Since the measured $V_g = 3,081$ m/sec of the empty aluminum shell is almost the same as the theoretical value, which is 3078 m/sec, in the following analysis we use the calculated phase velocity value, V_p, which is 2,190 m/sec. Furthermore, since the difference in V_p of the A_0 mode between the empty and water-filled shell is so small, in our estimate we use a constant V_p for both cases.

It is well known that when the incidence angle of a plane wave beam upon a solid plate satisfies the critical condition

$$\cos(\theta) = c_W / V_R, \qquad (4.2.2)$$

the transmitted wave is totally converted into a Rayleigh wave beam on the surface of the solid plate. In Eq. (4.2.2), c_W is the compression wave velocity in water, and V_R the Rayleigh wave velocity on the solid plate, respectively. Such a mode conversion phenomenon exists in other acoustical modes as well, for example, the A_0 mode in an aluminum plate immersed in water [57]. In this case the Rayleigh velocity V_R in Eq.(4.2.2) is replaced with the phase velocity of the A_0 mode, V_p^{A0}, in the solid plate.

For simplicity, we use the mode conversion picture described in [57] to interpret our experimental results in our case, for a thin-walled cylindrical aluminum shell filled with water. Here we use the quasi-plane wave approximation and acoustical ray method. We consider each ray radiated or leaked from a point on the shell as a plane wave beam with limited width, and ignore the slight variation within the beam width due to the curvature of the shell. Furthermore, the wave beams are represented by acoustic rays. Initially, the circumferential A_0 mode is excited efficiently by the transducer on the outer

surface of the shell. The A_0 waves propagate along the circumference, but can survive only for a limited distance in the shell due to strong leakage into the water. The A_0 mode wavevector, k_{A0}, is in the tangential direction along the circumference. The angle between k_{A0} and the wavevector of the compression wave, k_W, is given by

$$\cos(\theta) = c_W / V_p^{A0}, \tag{4.2.3}$$

where V_p^{A0} is the phase velocity of the A_0 mode for the water-filled shell. The "efficient distance" of the A_0 mode on the circumference, say within a loss in amplitude of -10 dB for example, depends on the emission angle and the mode-conversion coefficient, which is determined by the acoustic impedance of the shell material and of the water. According to [57], this distance is about 15 wavelengths for a plane aluminum plate in water (but how much loss in dB at 15 wavelengths is not mentioned). This distance is represented by arc AA' in Fig. 4.15. Rays radiating from arc AA', bounded by the rays in its vicinity, form an "effective" beam. When this beam arrives at the inner surface of the shell, it re-converts into A_0 mode in the shell because the wavevectors satisfy Eq.(4.2.2). The latter will start to emit into the water again.

For a fully filled shell, only rays following the paths in the hatched areas in Fig. 4.15 can be detected repeatedly and regularly. Note that all these paths have the same acoustical length in total, and thus rays following these paths all arrive at the transducer at the same time. So the detected echoes are the sum of these rays (plus their counterparts in the opposite direction, which fall in exactly the same hatched areas because of symmetry). These rays can be represented by an "effective beam" such as the one following the path
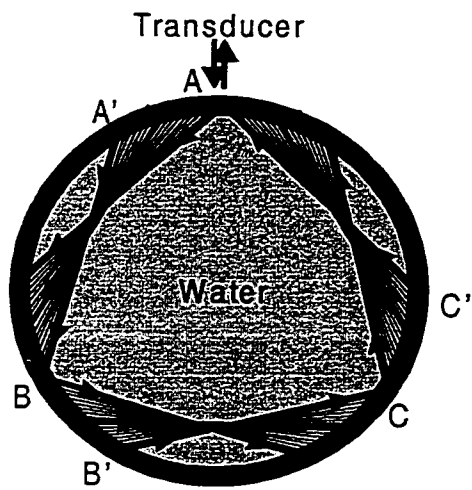
Fig. 4.15   Possible acoustical baths for detectable signals in a fully filled shell.
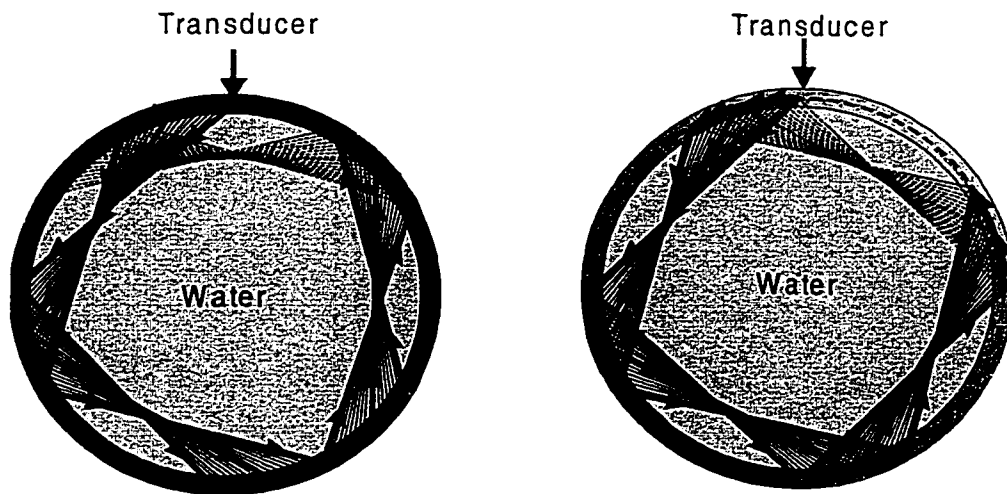
Fig. 4.16   Examples of acoustical baths for undetectable signals in a fully filled shell

AA'-A'B-BB'-B'C-CC'-C'A in Fig. 4.15. Compared to an acoustic lens, the arcs represent either an aperture or a focusing width.

For the 16.7% and 68.9% filled (in level) cases, the possible paths are illustrated in Fig. 4.17.
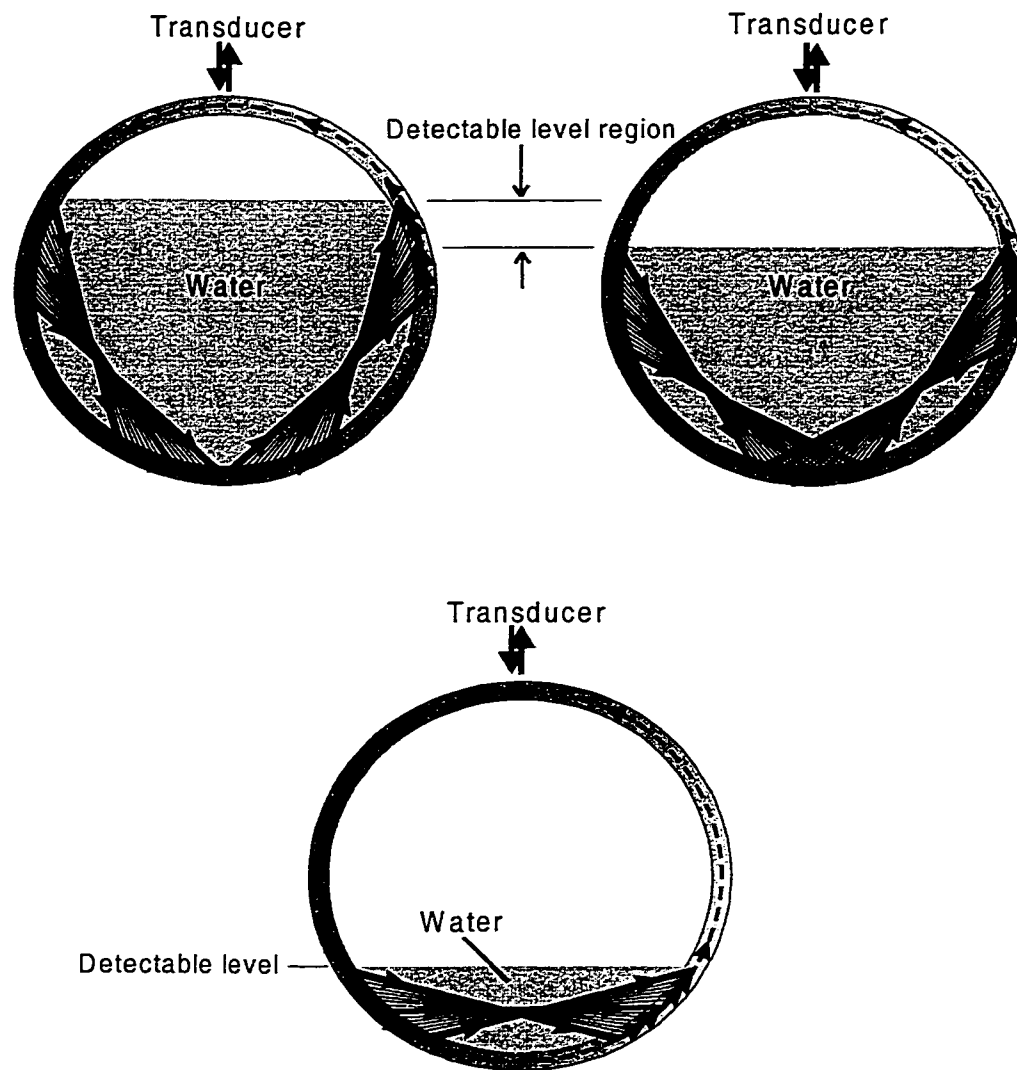
Fig. 4.17   Illustration of detectable water levels for a partially filled shell.

The periods for the wave beams to finish a complete path are calculated for the three typical cases:

a) Full;

b) 16.7% filled (in level);

c) 68.8% filled (in level).

Substituting into Eq. (4.2.3) V_p^{A0} =2,190 m/sec *at* 1MHz (fd=0.8 mm-MHz) and the compressive wave velocity in water c_W =1490 m/sec, the critical angle is estimated to be

$$\cos(\theta) = c_W / V_p^{A0} = \frac{1490}{2190}$$
$$\theta = 47.12°.$$

The wavelength at f = 1 MHz is about 2.2 mm. Given the critical angle, the length of one of the arcs in Fig. 13 is about 22 mm, or about 10 wavelengths long for the A_0 wave in the shell, which is a very reasonable "efficient distance" compared to that in [57].

The time delays for the three different levels calculated using the estimated θ value are listed in Table 4.1 with the measured data. They are in fairly good agreement. Fig. 4.18 also illustrates why for other level regions no regular echo trains could be observed.

Table 4.1   Measured and calculated delay time intervals in an aluminum cylindrical shell with an inner diameter of 91 mm and wall thickness of 0.8 mm, filled with different water levels.

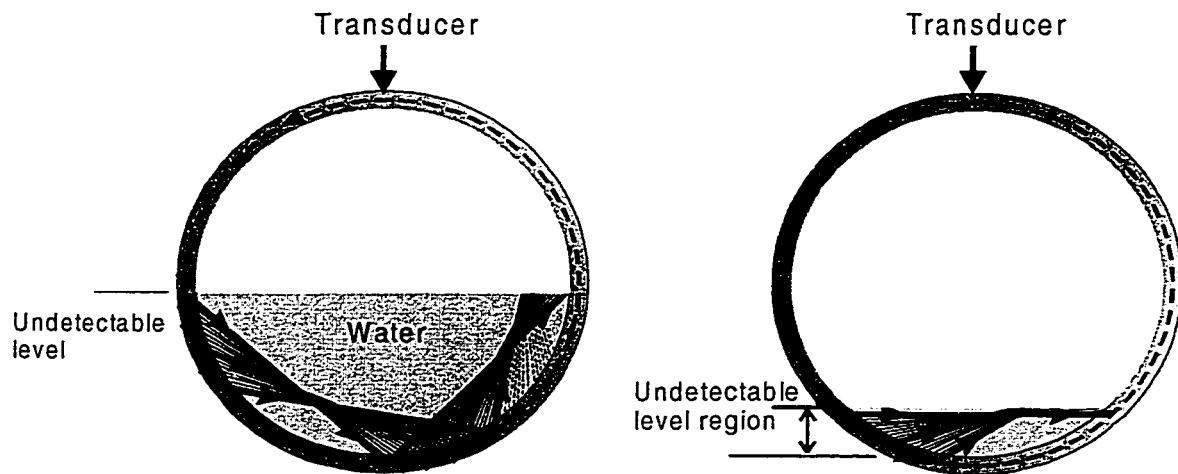| Filled Level	Measured time interval [μs]	Calculated time interval [μs]
Full	153.3	153.2
68.8%	135.1	133.4
16.7%	113.5	111.8
Empty	93.6	93.7 * * From the theoretical V_g

Fig. 4.18 Examples of undetectable water levels for a partially filled shell.

4.3 EMPTY AND WATER-FILLED BRASS TUBES

In addition to the stainless steel and aluminium tubes, experiments were also carried on brass tubes of different sizes. The combined contact and non-contact method shown in Fig. 3.6 was used for the measurement. Transducers of 1 MHz, 2 MHz, 5 MHz and 10 MHz were used. Clear and regular echo trains were obtained from both the thin-disk transducer and the laser probe in the empty brass tubes of all sizes at 1 MHz and 2 MHz. No appreciable signals were observed when 5 MHz and higher frequency transducers were used. Fig. 4. 19 shows the received signals at the same frequency for two empty brass tubes with the same thickness but different diameters. Note that the paired echoes received by the laser probe represent the signals from the two opposite directions around the tube circumference, due to the unequal distances between the transducer and the laser probing point, as shown in Fig. 3.4. At the same frequencies, no regular echoes were ever received in any of these brass tubes when they were filled with water.

This experiment was in fact performed before the two cases in Chap. 4.1 and 4.2. Although no interesting phenomenon was observed in these water-filled brass tubes, the measurement along with those on the stainless steel and aluminum tubes verified experimentally that the existence of circumferential wave propagation in a water-loaded tube depends not only on the frequency and the physical dimensions, but also on the materials of the tubes. This part was indeed also a very good exercise in transducer alignment and signal processing, which made the consequent experiments in the other two cases more smooth and productive.
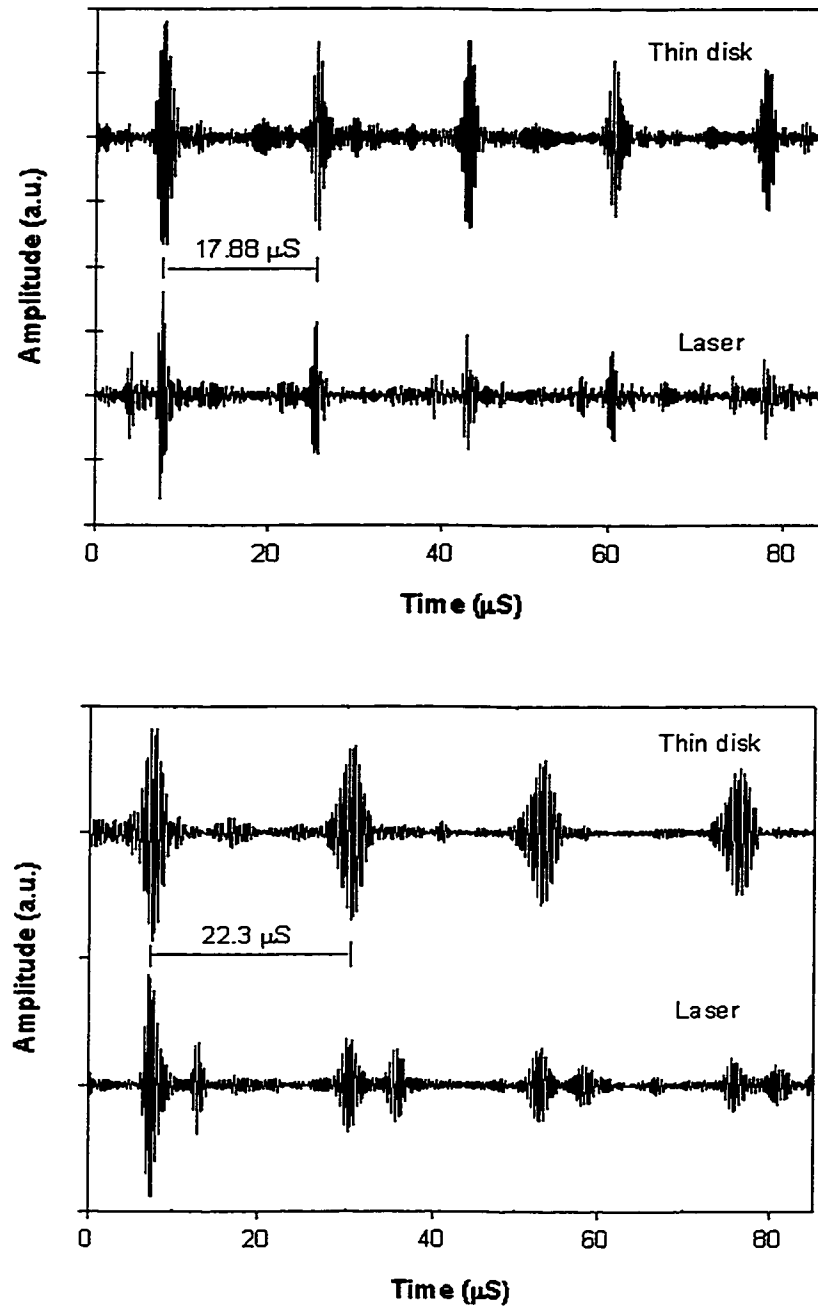
Fig. 4.19 Received time delay signals measured with a thin-disk transducer and a laser probe in brass tubes with wall thickness of 0.254 mm and diameters of 11. 89 mm (upper) and 15. 96 mm (lower) at 2.25 MHz.

CHAPTER 5. CONCLUSIONS

In this work we have studied theoretically and experimentally ultrasonic waves propagating in the circumference of empty and water-filled tubes.

In the theoretical modelling, we solved the wave equations separately for the two independent circumferential wave families. Dispersion relations of both the SH-type and Lamb-type circumferential modes were obtained.

From the asymptotic solutions, we show that the effect of the curvature on the SH-type waves in an empty tube is of second order, compared to the SH waves in a plate. For a tube with h/R << 1, the dispersion relations can take exactly the same form as its SH plate counterpart, by simply replacing the integer number m in all the expressions for the m-th order of the SH mode with $m' = m(1 + \delta_m)$, where $\delta_m = \frac{3}{2} \cdot \left(\frac{h}{2m\pi R} \right)^2$. The exact (numeric) solutions show that the difference between the dispersion curves of the SH circumferential modes and their plate counterparts are minimal. We also found that, unlike its plate counterpart SH_0, the lowest SH circumferential mode is not a constant and has a cut-off frequency.

We have also theoretically verified that the dispersion behaviour of the Lamb-type circumferential modes is very similar to that of their plate counterparts, with only slight difference in value at a given frequency. An exception is the asymptotic behaviour of the lowest antisymmetrical mode at zero frequency, which is significantly different from that of its plate counterpart, S_0. While the phase velocity of the S_0 plate mode remains constant as the frequency goes to zero, that of the S_0 circumferential mode goes to infinity. In other words, the S_0 circumferential mode has a "cut-off" frequency near

zero, while the S_0 plate mode has no cut-off frequency. As a result of this exception, the S_0 circumferential mode has a phase velocity equal to that of the bulk longitudinal wave at a frequency near zero, at which frequency the radial component of the displacement vector vanishes on the free surfaces of the tube. Such property makes the S_0 circumferential mode similar to all other antisymmetric circumferential modes and all non-zero order antisymmetric plate modes.

Experimentally, we have developed a novel technology which has superior advantages over many existing methods for experimental determination of the dispersion of circumferential waves. With a chirp interdigital transducers (IDT) as a broadband transmitter and receiver integrated on a stainless steel tube coated with piezoelectric film, we successfully generated and detected Lamb-type circumferential waves in the tube with very good signal-to-noise ratio over a significantly wide frequency range, which covered the most sensitive region of the lowest flexural mode.

The experimental group velocity and phase velocity were in excellent agreement with the theoretical values for the empty tube. In a water-filled stainless steel tube we have unambiguously observed propagation of tube-born rather than water-born circumferential waves. The group velocity spectrum is significantly different from that for an empty tube. Although our own theoretical modelling is not sufficient to interpret the observed mode(s), all experimental evidence strongly suggests that the waves are related to the flexural motion in the water-loaded tube system. The phenomenon may be best interpreted as a result of the strong interaction between the lowest flexural circumferential tube mode, A_0, and the first two S-shaped Whispering Gallery modes, the latter being newly predicted with the resonant scattering theory by Veksler *et al.* and

Maze [55, 56]. In other words, with our unique configuration we may have experimentally observed for the first time the presence of the new circumferential modes in a water-filled stainless steel tube, which reflect the flexural motion of the compound tube-water system. Experimental observation of these modes has not hitherto been reported and is difficult if not impossible in any other documented configurations. The discrepancy between the experiment and the theory in value and in detailed dispersion trends may be due to experimental uncertainty and the parameters used. A conclusive identification of these new modes in the given configuration will need more careful experiments and precise computations.

In a water-filled aluminum shell we have also observed mode conversions between the lowest flexural mode in the shell and the compressional waves in the water. A partially filled shell with a horizontal central axis was fully investigated. The experimental results were satisfactorily described with the quasi-plane wave approximation and acoustical ray method.

In both the typical experiments for the water-filled stainless steel tube and the water-filled aluminium shell, the measured delay time intervals show a very large changes from the empty cases. Although different mechanisms are responsible for the large changes, the phenomenon in both cases show good application potentials in liquid level sensing.

REFERENCES

1. X. Li, *Ultrasonic Thin Walled Tube Wave Devices*, M.Sc. thesis, Concordia University, 1994.

2. X. Li, Z. Wang, C.K. Jen, M. Viens and J.D.N. Cheeke, "Ultrasonic thin-walled tube wave structure for sensing devices," IEEE Trans. Ultrason., Ferroelect., Freq. Contr., **43** (2), 331-336 (1996).

3. X. Li, Z. Wang, C.K. Jen, M. Viens and J.D.N. Cheeke , "Ultrasonic thin wall tube wave devices for sensor consideration," Appl. Phys. Lett, **67**, 37-39 (1995).

4. J.D.N. Cheeke, X. Li and Z. Wang, "Characteristics of circumferential waves in thin walled tube acoustic devices," 1995 Proc. IEEE Ultrason. Symp., 441- 444 (1995).

5. Lord Rayleigh, "On the free vibrations of an infinite plate of homogeneous isotropic elastic matter," Proc. Lond. Math. Soc. **20**, 225- (1889).

6. H. Lamb, "On the flexure of an elastic plate," Proc. Lond. Math. Soc. **21**, 85- (1889).

7. H. Lamb, "On waves in an elastic plate," Proc. Roy. Soc. A **93**, 114-128 (1917).

8. M.F.M. Osborne and S.D. Hart, "Transmission, reflection and guiding of an exponential pulse by a steel plate in water. I. Theory", J. Acoust. Soc. Am. **17**, 1-18 (1945).

9. J. W. C. Sherwood, "Propagation in an infinite elastic plate," J. Acoust. Soc. Am. **30**, 979-984 (1958).

10. I.A. Victorov, "Ultrasonic Lamb waves (review)," Sov. Phys. Acous. **11**, 1-14 (1965).

11. I.A. Victorov, *Rayleigh and Lamb Waves: Physical Theory and Applications* Plenum Press, New York (1967).

12. H. Überall, "Surface waves in acoustics," in *Physical Acoustics*, ed. by W.P. Mason and R.N. Thurston, Vol. X (Academic Press, New York 1970).

13. B.A. Auld, "Rayleigh wave propagation," in *Rayleigh-Wave Theory and Application*, ed. by E.A. Ash and E.G.S. Paige (Springer-Verlag, Berlin Heidelberg 1985), pp. 12-27.

14. G. Maze, L. Izibicki and J. Ripoche, "Resonance of plate and cylinders: Guided waves", J. Acoust. Soc. Am. **77** (4), 1352-1357 (1985).

15. T.J. Matula and P.L. Marston, "Energy branching of a subsonic flexural wave on a plate at an air-water interface. I. Observation of the wave held near the interface and near the plate", J. Acoust. Soc. Am. **97**, 1389-1398 (1995).

16. H. Dabirikhah, and C.W. Turner, "The coupling of the A_0 and interface Scholte modes in fluid-loaded plates", J. Acoust. Soc. Am. **100** (5), 3442-3445 (1996).

17. H.L. Bao, R.K. Franklin, P.K. Raju and H. Überall, "The splitting of dispersion curves for plates fluid-loaded on both sides", J. Acoust. Soc. Am. **102** (2), 1246-1248 (1997).

18. D.C. Gazis, "Exact analysis of the plane-strain vibrations of thick-walled hollow cylinders," J. Acoust. Soc. Am. **30**, 786-794 (1958).

19. H.I. Epstein, "Circumferential waves for a cylindrical shell supported by a continuum," J. Sound Vib. **58**, 155-166 (1978).

20. N.D. Veksler, "Dispersion curvers for the phase velocities of Lamb-type circumferential waves excited in a circular cylindrical shell in the scattering of a plane acoustic wave by the shell," Sov. Phys. Acoust. **35** (6) 600-602 (1989).

21. N.D. Veksler, "The analysis of peripheral waves in the problem of plane acoustic pressure wave scattering by a circular cylindrical shell," Acustica **69**, 63-72 (1989).

22. G.C. Gaunaurd and D. Brill, "Acoustic spectrogram and complex frequency poles of a resonantly excited elastic tube," J. Acoust. Soc. Am. **75**, 1680-1693 (1984).

23. E.D. Breitenbach, H. Überall and K.B. Yoo, "Resonant scattering from elastic cylindrical shells," J. Acoust. Soc. Am. **74**, 1267-1273 (1983).

24. M. Talmant, H. Überall, R.D. Miller, M.F. Werby and J.W. Dickey, "Lamb waves and fluid-borne waves on water-loaded, air-filled thin spherical shells," J. Acoust. Soc. Am. **86** (1), 278-289 (1989).

25. M. Talmant and G. Quentin, "Backscattering of short ultrasonic pulse from thin cylindrical shells," J. Appl. Phys. **63** (6), 1857-1863 (1988).

26. M. Talmant, G. Quentin, J.L. Rousselot, J.V. Subrahmanyam and H. Überall, "Acoustic resonances of thin cylindrical shells and the resonance scattering theory," J. Acoust. Soc. Am. **84** (2), 681-688 (1988).

27. J.-L. Izibicki, G. Maze and J. Ripoche, "Diffusion acoustique par des tubes immerges dans l'eau Nouvelles resonances observees en basse frequence', Acustica, **61**, 137-139 (1986).

28. P. Pareige, G. Maze et J. Ripoche, "Resonances d'un tube elastique: source d'emission acoustique interne," Revue de physique appliquee, **22**, 83-88 (1987).

29. A. Gérard, J.L. Rousselot, J.-L. Izibicki, G. Maze and J. Ripoche, "Resonances d'ondes d'interface de coques cylindriques minces immerges: determination et interpretation", Revue de physique appliquee, **23**, 289-299 (1988).

30. R.D. Doolittle, H. Überall and P. Ugincius, "Sound scattering by elastic cylinders," J. Acoust. Soc. Am. **43**, 1-14 (1968).

31. L. Fax, L.R. Dragonette, and H. Überall, "Theory of elastic resonance excitation by sound scattering," J. Acoust. Soc. Am. **63**, 723-731 (1978).

32. G.S. Sammelmann, D.H. Trivett and R.H. Hackman, "The acoustic scattering by a submerged, spherical shell. I: The bifurcation of the dispersion curve for the spherical anti-symmetric Lamb wave", J. Acoust. Soc. Am. **85** (1), 114-124 (1989).

33. J.W. Dickey and H. Überall, "Surface wave resonances in sound scattering from elastic cylinders", J. Acoust. Soc. Am. **63**, 319-320 (1978).

34. Y. Liu and L.C. Lynnworth, "Flexural wave sidewall sensor for noninvasive measurement of discrete liquid levels in large storage tanks," 1993 Proc. IEEE Ultrason. Symp., 385-390 (1993).

35. G.C. Ganaurd, "The sonar cross section of a coated hollow cylindeer in water", J. Acoust. Soc. Am. **61**, 360-368 (1971).

36. M.S. Choi, M.S. Yang and H.C. Kim, "Detection of leak-defective fuel rods using the circumferential Lamb-waves excited by the resonance backscattering of ultrasonic pulses," Ultrasonics, **30**, 221-223 (1992).

37. A Pilarski, J.J. Ditri, and J.L. Rose, "Remarks on symmetric Lamb waves with dominant longitudinal displacements," J. Acoust. Soc. Am. **93** (4), 2225-2230 (1993).

38. D.R. Hull, H.E. Kautz, and A. Vary, "Measurement of ultrasonic velocity using phase-slope and crosscorrelation methods".

39. J.-P. Monchalin, "Optical detection of ultrasound," IEEE Trans. Ultrason., Ferroelect., Freq. Contr., **33** (5), 485-489 (1986).

40. J.-P. Monchalin, J.-D. Aussel, R. Héon, C.K. Jen, A. Boudreault, and R. Bernier, "Measurement of In-Plane and Out-of-Plane by Optical Heterodyne Interferometry," J. Nondestr. Eval. **8** (2), 121-133 (1989).

41. J.-D. Aussel and J.-P. Monchalin, "Study of surface acoustic wave dispersion using laser-ultrasonics and application to thickness measurement," in Review of Progress in Quantitative NDE (Vol. 8), D.O. Thompson and D.E. Chimenti, eds. (Plenum Press, New York (1989), p. 535-542.

42. R. Stoneley, "Elastic waves at the interface of separation of two solids," Roy. Soc. Proc. London, **A 106**, 416-428 (1924).

43. L. M. Brekhovskikh, "Surface waves confined to the boundary in solids," Sov. Phys. Acous. 13, 462- (1968)

44. Lord Rayleigh, "Whispering Galleries," Section 287, *The Theory of Sound* 2 (MacMillan, London 1896, 2nd Ed.), 126.

45. O.D. Grace and R.R. Goodman, "Circumferential waves on solid cylinders," J. Acoust. Soc. Am. **39**, 173-174 (1966).

46. H.I. Epstein, "Circumferential waves in a composite circular cylinder," J. Sound Vib. **48**, 57-71 (1976).

47. R.E. Bunny and R.R. Goodman, "Rayleigh and Lamb waves on cylinders," J. Acoust. Soc. Am. **46**, 1223-1227 (1966).

48. I.A. Victorov, "Rayleigh-Type waves on a cylindrical surface," Sov. Phys. Acoust. **4**, 131-136 (1958).

49. I.A. Victorov and O.M. Zubova, "Normal plate modes in a solid cylindrical layer," Sov. Phys. Acoust. **9**, 15-17 (1963).

50. I.A. Victorov, E.K. Grishchenko, and T.M. Kaekina, "An investigation of the propagation of ultrasonic surface waves at the boundary between a solid and a liquid," Sov. Phys. Acoust. **9**, 131-137 (1963).

51. I.A. Victorov, "Calculation of the phase velocities of surface waves on the boundary of a solid half-space with a liquid layer," Sov. Phys. Acoust. **23**, 541-542 (1977).

52. N.D. Veksler, J.-L. Izbicki, and J.-M. Conoir, "Bending A waves in the scattering by circular cylindrical shell: its relation with the bending free modes," J. Acoust. Soc. Am. **96** 287-293 (1994).

53. J. Metsaveer and A. Klauson, "Influence of the curvature on the dispersion curves of a submerged cylindrical shell," J. Acoust. Soc. Am. **100** , 1551-1560 (1996).

54. J.D.N. Cheeke, X. Li and Z. Wang, "Observation of flexural lamb waves (A_0 mode) on water-filled cylindrical shell," J. Acoust. Soc. Am. **104** (6), 3678-3680 (1998).

55. N.D. Veksler, J.-L. Izbicki, J.-M. Conoir, "Flexural waves at acoustic wave scattering by a liquid-filled cylindrical shell," in private communication, to be submitted for publication (1999).

56. G. Maze, private communication (1999).

57. M.O. Deighton, A.B. Gillespie, R.B. Pike and R.D. Watkins, "Mode conversion of Rayleigh and Lamb waves to compression waves at a metal-liquid interface," Ultrasonics, **19**, 249-258 (1981).

58. A.B. Gillespie, M.O. Deighton, R.B. Pike and R.D. Watkins, "A new ultrasonic technique for the measurement of liquid level," Ultrasonics, **20**, 13-17 (1982).

59. S.G. Solomon, H. Überall and K.B. Yoo, "Mode conversion and resonant scattering of elastic waves from a cylindrical fluid-filled cavity," Acustica **55**, 147-159 (1984).